

Department of Construction Sciences

Solid Mechanics

ISRN LUTFD2/TFHF-18/5224-SE(1-77)

Wrinkling in packaging material: Experiments and thermo-mechanical stochastic modeling

Master's Dissertation by

David Johansson

and

Linus Dahlström

Supervisors:

M. Sc. Eskil Andreasson, Tetra Pak®

M. Sc. Viktor Petersson, Tetra Pak®

Assoc. Prof. Stephen Hall, Div. of Solid Mechanics

Examiner:

Prof. Matti Ristinmaa, Div. of Solid Mechanics

Copyright © 2018 by the Division of Solid Mechanics

David Johansson and Linus Dahlström

Printed by Media-Tryck AB, Lund, Sweden

For information, address:

Division of Solid Mechanics, Lund University, Box 118, SE-221 00 Lund, Sweden

Webpage: www.solid.lth.se

Acknowledgements

We would like to start off by thanking our three supervisors for assisting us throughout this semester with our thesis work and for preparing us for future endeavors. M. Sc. Eskil Andreasson has aided us every step of the way and always made sure that we had a proper outlet to vent questions and discuss results. Viktor Petersson has helped us with modeling issues, as well as with the majority of all practical necessities. Assoc. Prof. Stephen Hall has used his extensive experience to help us utilize and interpret X-ray computed tomography.

Magnus Lindvall and Johan Nordgren from Altair have always answered every single one of our infinite amount of questions regarding modeling and software application. Without the two of you, there would exist no virtual model.

Mujtaba Al-Ibadi, Henrik Askfelt, Eric Borgvist, Tommy Lindström, Milena Minovic, Anders Olin, Dag Svärd, Madeleine Svärdby and Johan Tryding are just some of all the people having been involved in helping to move our thesis along and we would like to express our sincere gratitude to you all.

Lastly a large debt of gratitude is owed to Sofia Wiktorsson for support and encouragement during every day, from start to finish.

Abstract

As one of the world leaders in food packaging, it is in the interest of Tetra Pak® to increase the understanding of packaging material and how it can better be virtually modeled, using finite element (FE) simulations. The aim of this thesis is to evaluate whether a stochastic approach can be taken to generate a more realistic response than a purely deterministic one, in the aforementioned models. To accomplish this, a load case involving the exposure of packaging material to excessive heating is investigated, physically as well as virtually.

The physical experiments consist of thermally loading small samples of packaging material with the in-plane dimensions 3 mm × 25 mm using a heat gun and analyzing the results, both by ocular inspection and by using X-ray computed tomography. The virtual experiments consist of pre-processing in the computer software HyperMesh, using Abaqus as an FE-solver and HyperView and Abaqus as post-processors, to replicate the results, by implementing a realistic paperboard surface topography.

The conclusion from the virtual results is that the chosen stochastic approach in this thesis can be used to capture microstructural phenomena, such as the buckling of the thin thermally expanded aluminum foil of the packaging material. The different virtual experiments do, however, not always match the physical ones, and may need further improvement.

Future works could include a more systematic and controlled environment for the experiments, i.e. a testing rig with greater repeatability and with the possibility of easily varying the parameters of the system.

Sammanfattning

Som ett av de mest framstående företagen inom livsmedelsförpackning, är det av intresse för Tetra Pak[®] att öka förståelsen kring förpackningsmaterial och hur man kan modellera detta bättre virtuellt, m h a finita element-simuleringar. Målet med denna avhandling är att utvärdera huruvida ett stokastiskt tillvägagångssätt kan användas för att generera mer realistiska resultat än ett deterministiskt, i dessa modeller. För att åstadkomma detta så kommer ett lastfall som involverar termisk belastning undersökas, både fysiskt och virtuellt.

De fysiska experimenten består av att termiskt belasta små provbitar av förpackningsmaterial med dimensionerna 3 mm × 25 mm med en värmepistol och analysera resultaten, både genom ockulär inspektion och med datortomografi. De virtuella experimenten bestod av att pre-processera i HyperMesh, använda Abaqus' FE-lösare och HyperView samt Abaqus som post-processorer, för att även replikera resultaten, genom att implementera en realistisk yttopografi hos kartongen.

Slutsatsen från de virtuella resultaten är att det stokastiska tillvägagångssättet i denna avhandling kan användas för att fånga mikrostrukturella fenomen, såsom knäckning av den tunna, värmeutvidgade aluminiumfolien i förpackningsmaterialet. De olika virtuella experimenten överensstämmer dock inte alltid med de fysiska och behöver förbättras ytterligare.

Framtida arbete inom detta område skulle kunna utgöras av en mer systematisk och kontrollerad miljö för de fysiska experimenten, d v s en rigg med högre repeterbarhet och med möjlighet att lättare variera systemets parametrar.

Contents

1	Introduction	1
1.1	Background	1
1.2	Thesis objectives	3
1.3	Delimitations and assumptions	4
1.4	Scope of the thesis	5
2	Theory	6
2.1	Packaging material	6
2.2	Thermal physics	8
2.3	Buckling	11
2.4	Constitutive modeling	13
2.5	Stochastic modeling	21
3	Method	26
4	Experiments and measurements	30
4.1	Physical experiments	30
4.2	Image analysis	42
5	Virtual experiments	50
5.1	Model	51
5.2	Results	57
5.3	Analysis	61
6	Comparison and Conclusion	64
7	Future work	68
	References	71
A	Appendix	74

1 Introduction

Tetra Pak[®] is a Swedish company that was established back in 1940 by Dr. Ruben Rausing. It started off as a company with a vision to create paper-based packaging used for storing milk hygienically, with as little material as possible. From there it has grown to become a multinational company, focusing on solutions for processing and packaging all kinds of food and beverages. The company develops and manufactures packaging material and supply the complete packaging solution, including the entire machinery. With over 24,000 employees all over the world, their products reach the market of over 170 countries on a daily basis [1].

The work behind this thesis took place in the group Packaging Development at Packaging Technologies, Packaging Solutions at Tetra Pak[®] Råbyholm in Lund, as well as at Lund University at the Division of Solid Mechanics.

1.1 Background

How to create discrete approximations of continuous physical models in the form of finite elements (FE) is well known, when dealing with macrostructure. The finite element method is the most common numerical way of solving differential equations on complex geometries and is widely used and implemented in numerable commercial software. At Tetra Pak[®] deterministic models based on this methodology are thoroughly investigated and frequently adopted in research and development of new packaging technologies, packaging solutions and in the improvement of old ones. A deterministic model is a model that will generate the same output from a given initial input, i.e. no randomness is involved.

When modeling structures, where the least bit of disturbance causes vast differences, deterministic virtual models may not generate a realistic response. Phenomena such as buckling and the instability of bar-systems (described by Krenk [2]) depend heavily on subtle changes in geometry and the direction of forces, and a slight change in these

can severely alter the outcome of a process. This type of process might benefit from a stochastic approach, such as introducing different imperfections into a system, to see how this affects the outcome of a loading scenario. The effect of such seemingly stochastic behavior is the focus of this thesis. In contrary to a deterministic model, a stochastic model takes randomness into consideration. This means that a given input does not always generate the same output, due to inherent randomness of the model. Accomplishing the solving of the same system of equations and simultaneously incorporating a stochastic component has historically been done by implementing the Stochastic Finite Element Method (SFEM) [3][4].

In this Master's thesis FE-simulations are used to try to replicate a physical experimental setup. The experimental setup consists of heating small strips of packaging material. In experiments devised by Askfelt and Ristinmaa [5], it has been observed that, prior to what is referred to as "blister"-formation in this article (Fig. 1.1), a small irregular elevation forms.

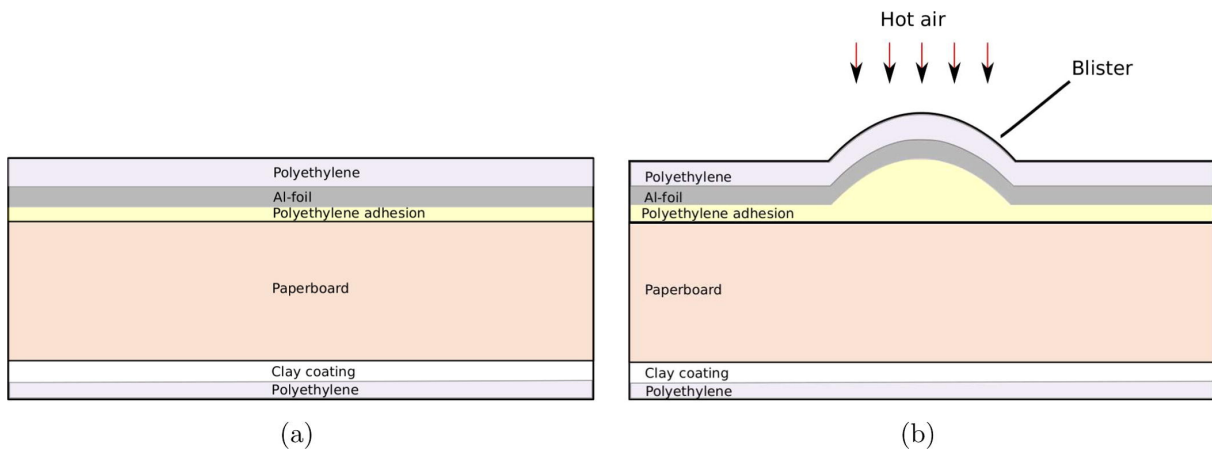


Figure 1.1: Conceptual model for blister formation in paperboard due to moisture escaping the fibers of the paperboard [5].

The experiments of this thesis focus on these irregular elevation (Fig. 1.2) and whether they can be recreated in an FE-model.

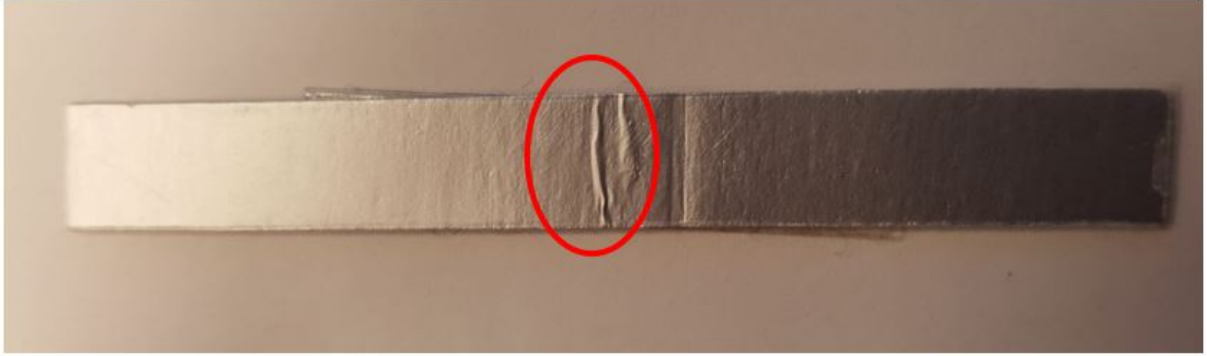


Figure 1.2: Wrinkle on a 3 mm \times 25 mm sample of packaging material, having been exposed to thermal loading.

A similar phenomenon has previously been investigated in different scientific articles. In 2005, for instance, Huang looked at the evolution of wrinkles in elastic-viscoelastic bilayer thin films [6]. Huang found that the viscoelastic properties of the substrate had a big impact on the stability and kinetics of the wrinkling process.

1.2 Thesis objectives

The purpose of this thesis is to increase the knowledge of how small variations, i.e. stochastic changes, in geometry, forces or boundary conditions can change the outcome of a loading scenario. The thesis focuses on small FE-models, where coupled thermo-mechanical responses are expected. An array of experiments are conducted to validate a virtual representation of a certain load case. X-ray computed Tomography (XCT) images are used to further understand the physics behind this specific case. These images are also used to implement a realistic microstructure and make the virtual model even more receptive to validation by real experiments. The objectives of the thesis are:

- Using a series of experiments, investigate how packaging material responds to thermal loading with respect to thermal expansion.
- Create a virtual model, using some form of stochastic approach to mimic e.g. the topography of paperboard.

- Use the results of these physical experiments to validate the adequacy of the virtual experiments.
- Use XCT to construct images of a packaging material specimen before and after exposing it to a specific thermal load, to gain greater understanding of the process.

1.3 Delimitations and assumptions

Some simplifying assumptions and delimitations were made, to usher the process along smoothly.

- The experiments have been limited to encompass only the most relevant parameters and mainly for one type of packaging material. Instead of trying all possible values, the parameters were assigned extreme values, to demonstrate how it affected the outcome, without quantifying too much.
- Due to lack of a suitable rig, semi-manual experiments had to be performed, diminishing the precision of the system.
- The simulations of the virtual models were a time-consuming process, why some simplifications were made, when creating the virtual model. The coating of clay, used to make the application of decor easier, and the decor polymer layer (see Chapter 2.1) were excluded, since they were located on the other side of the paperboard and therefore assumed not to affect the phenomenon to any significant extent.
- The thermal expansion of the aluminum foil and the polymer were assumed to be of a constant, isotropic character.
- The theory reviewed regarding stochastic modeling was not implemented, but merely used as guidelines.
- No plasticity model was implemented for the paperboard, as it was not expected to be exposed to stresses of a magnitude high enough.

1.4 Scope of the thesis

The disposition of the thesis is constructed to make it easy for the reader to understand the physics and mathematics involved in the experiments, both physical and virtual, and to describe the progression of the thesis work and results in an as concise and structured way as possible. The second chapter contains the theory believed to govern the phenomena of the specific load case. This chapter also introduces some minor numerical approaches. Chapter 3 contains a summary of the methodology used during the project, i.e. how, in broad strokes, the planning and workflow were carried out. The fourth and fifth chapter illustrate how the physical and virtual experiments respectively, were conducted, along with the results this yielded and what may be concluded. Chapter 6 offers a comparison between the results from the physical and virtual experiments. Chapter 7 contains a brief summary of what may be done in the future to further improve the techniques used here.

2 Theory

In this chapter, theory regarding the physics related to the phenomena observed in the physical and virtual experimenting are discussed. It starts off with a description of packaging material and continues on to review the physics behind the thermal loading investigated in this thesis. A discussion regarding the derivation of the FE formulation, thermo-plasticity and the coupled thermo-mechanical constitutive equations are omitted, owing to their respective size. The last part focuses on stochastic modeling and how it has been implemented historically.

2.1 Packaging material

Packaging solutions created by Tetra Pak[®] have different material structure. A combination of polymer, aluminum and paperboard is used to make each type of package as suitable as possible for the product it contains. Some packages are developed for products that do not need a long durability and therefore do not need as many layers as, for example, an aseptic container does.

All different layers serve a specific purpose. A schematic picture of the cross-section of a typical package can be seen in Fig. 2.1. At the innermost boundary (to the left in Fig. 2.1) a polymer layer protects the product itself. This layer, as well as the rest of the polymer layers, consists of polyethylene. It is connected to an aluminum layer through an adhesive layer, which is shown as the second polymer layer from the left in Fig. 2.1. The purpose of the aluminum is to prevent light and oxygen from reaching the product. This contributes to making the package aseptic. Next is the laminate layer, which is another polymer layer, that acts as an adhesive, adhering the aluminum to the paperboard. The paperboard constitutes the stability of the package. It is usually divided into three different parts, where the middle part is less compact than the top and bottom part. The reason for this is to decrease the total paperboard weight, but still maintain a high bending stiffness, similar to the idea behind an I-beam. The printing and graphics is applied to the outermost paperboard

boundary (to the right in Fig. 2.1). Between this and the final layer of polymer, a layer of clay is generally included, to create a smoother surface to allow for a better looking print. However, this layer is not included in Fig. 2.1. At the outermost edge there is a final layer of polymer that protects the package from moisture. This layer is also called the décor layer.

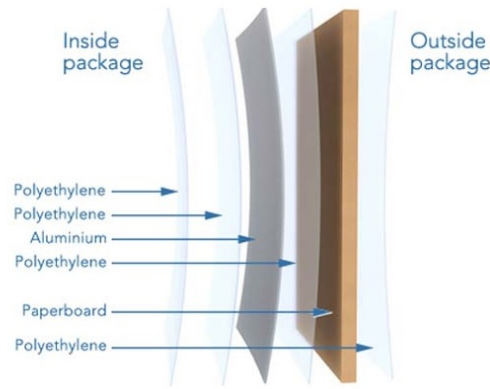


Figure 2.1: The different layers in a typical Tetra Pak package [7].

The paperboard component of the packaging material is *anisotropic*, meaning that it has different properties in each direction. However, it turns out that assuming that it is *orthotropic* is often sufficient and is therefore done for the remainder of this thesis. Orthotropic means that the material has different properties along each axis in an orthonormal coordinate system. The three directions of the paperboard is referred to as machine direction (MD), cross direction (CD), and out-of-plane direction (ZD) according to Figure 2.2.

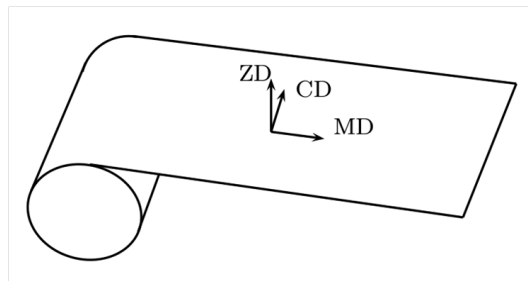


Figure 2.2: The three material directions of paperboard.

For the layers not to fall apart, the structure of the interfaces between the different

materials is essential. This is described above in passing as "adhesion". The effect of thermal loading combined with delamination between paperboard and polymer are investigated in this thesis.

2.2 Thermal physics

The transfer of heat is often divided into three separate categories: thermal conductivity, thermal radiation and thermal convection. In this thesis the focus is on just thermal conduction, considering the remaining two to be negligible, in the time-scale used in the simulations of this thesis.

Heat equation

To describe how the heat is evolving throughout a material the following differential equation is used

$$\frac{\partial u}{\partial t} - a\Delta u = \frac{a}{\lambda}k \quad (2.1)$$

where u is a function of the spatial variables as well as time, i.e.

$$u = u(x, y, z, t) \quad (2.2)$$

This partial differential equation (PDE) describes how the temperature u varies with time t in a given region and is known as the heat equation. Here, a is the thermal diffusivity, λ is the thermal conductivity and k is the applied heat per unit time and unit volume. The strategy used for solving these equations generally depends on the relevant geometry on which the equation is applied, as well as the given boundary conditions. The solution is easily calculated analytically or by using tables for geometries such as rods, cubes and spheres, using Fourier series expansion as well as Bessel-functions, but when more complicated structures are involved numerical methods are required [8][9]. Using the finite element method, the transient part has to be

handled before proceeding with further discretization. If Eqn. 2.1 is sampled at time t_{n+1} this can be written as

$$\left(\frac{\partial u}{\partial t}\right)^{n+1} - \alpha \nabla^2 u^{n+1} = \left(\frac{a}{\lambda} k\right)^{n+1} \quad (2.3)$$

Each time-step depends on the previous one. This equation can be solved using both implicit and explicit methods, two of the most prominent ones being Euler backward and Euler forward, respectively. The difference between the two is the assumption made regarding the first term. An implicit assumption will result in writing

$$\left(\frac{\partial u}{\partial t}\right)^{n+1} = \frac{u_{n+1} - u_n}{\Delta t} = \alpha \nabla^2 u^{n+1} + \left(\frac{a}{\lambda} k\right)^{n+1} \quad (2.4)$$

while the explicit one says that

$$\left(\frac{\partial u}{\partial t}\right)^{n+1} = \frac{u_{n+1} - u_n}{\Delta t} = \alpha \nabla^2 u^n + \left(\frac{a}{\lambda} k\right)^n \quad (2.5)$$

The explicit solver in Abaqus, used in this thesis, utilizes two similar methods, called the central-difference integration rule and the forward-difference integration rule, when solving the mechanical and thermal equations, respectively [10][11].

Thermal Expansion

Central to understanding deformation of the aluminum layer in the packaging material is thermal expansion. This is described in one dimension by

$$\alpha_L \Delta T = \frac{\Delta L}{L} \quad (2.6)$$

where T is the temperature, L is the length and Δ denotes the difference between two states. α_L is the coefficient of thermal expansion for a one-dimensional geometry, see

Fig. 2.3.

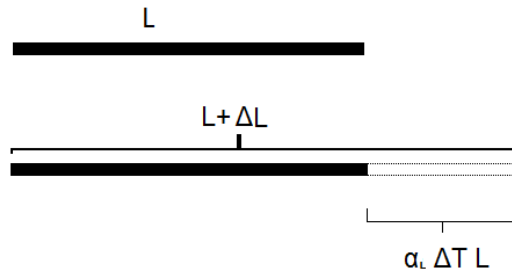


Figure 2.3: The upper image shows a 1-D bar of a material with the coefficient of thermal expansion α_L . The image at the bottom shows the same bar being ΔL m longer, after being heated ΔT °C.

The value of α_L depends on the material. For a cubic element with the same α_L along all material axes (isotropic thermal expansion) one can write

$$V + \Delta V = (L + \Delta L)^3 = L^3 + 3L^2\Delta L + 3L\Delta L(\Delta L) + (\Delta L)^3 \quad (2.7)$$

which, if ΔL is small and remembering that $L^3 = V$, may be re-written as

$$V + \Delta V = V + 3L^2\Delta L \quad \implies \quad \frac{\Delta V}{V} = 3\frac{\Delta L}{L} = 3\alpha_L\Delta T = \alpha_V \quad (2.8)$$

where α_V is the volumetric thermal expansion. The aluminum used in the modeling was considered to be isotropic with respect to thermal expansion, i.e. $\alpha_{11} = \alpha_{22} = \alpha_{33} = \alpha_L \approx 20 \times 10^{-6} \text{ K}^{-1}$ and $\alpha_{12} = \alpha_{13} = \alpha_{23} = 0$. The thermal expansion of the polymer was also considered to be isotropic. The thermal expansion of the paperboard was deemed irrelevant and was therefore omitted.

2.3 Buckling

The definition of the physical phenomena known as buckling can be illustrated by the simple case of a brace being subjected to an axial load. When the load reaches a certain critical value the brace starts bending out in a direction different from that of the applied force, see Fig. 2.4. Any small increase in the loading after this point will generate a relatively large change in deformation [12].



Figure 2.4: (a) shows a brace subjected to a force P , before buckling begins. (b) shows a brace subjected to a slightly larger force P , causing it to buckle.

Buckling is present in many areas of physics. For instance, it can be observed on railway tracks, where it is called heat distortion, and consists of local horizontal buckling of the rail. The underlying cause is often large forces, or weakened stability, due to ballast failure in the railroad track. It is usually triggered by the heat of the sun (thermal expansion) and develops when the rail fails to withstand the forces acting in the direction of the rail [13], as shown in Fig. 2.5 (a). Buckling can also be found in nature. In big rock structures what is called *active folding* can be observed. The buckling of different stone layers can be seen very clearly, as is illustrated in Fig. 2.5 (b).



(a) Buckling of railroad track due to thermal expansion [13].



(b) Active folding in rock [14].

Figure 2.5: Buckling phenomena within other physical disciplines.

The phenomenon is usually initiated when a layer is shortened parallel to the layering. This is active folding, responding to the imposed stress field. A requirement for buckling to occur is a contrast in viscosity between the folding layer and the host rock, the folding layer being the more competent of the two. Competence refers to the degree of resistance of rocks. However, a condition for buckling to occur is that irregularities are present in the layer interfaces. These irregularities can then grow to form *buckle folds* with a shape and size that depend on the thickness of the folded layer, but also on the contrast of viscosity to the surroundings. An isotropic rock layer, however, with perfectly planar and parallel boundaries, will shorten without folding, despite the fact that there is a significant contrast in viscosity between the layer and the host rock [15].

Buckling is mainly associated with larger constructions, but has also been found to play a part in thin sheets of metal being subjected to stress, more akin to what is investigated in this thesis [6][16].

The phenomenon investigated in this thesis is thought to be caused by buckling of the aluminum layer in the packaging material. This results in what resembles a "wrinkle" in the material. Hence, from here on the phenomenon will be referred to as "wrinkling/buckling" and the result as a "wrinkle". An example of a wrinkle is shown in Fig. 1.2.

2.4 Constitutive modeling

Being able to create virtual models describing the effect of the microstructure, i.e. the surface topography, is central to this thesis, and this warrants an introduction to some of the theory behind constructing constitutive models. Relevant to the virtual experiments was the plasticity model of the aluminum foil, which had been created previous to this thesis. Below follows a summary of some of the theory needed to construct such a model, as well as some general comments on theory regarding small deformations. The FE-formulation, thermo-plasticity and the theory behind thermo-mechanical coupling was omitted, and the reader is referred to the Abaqus documentation as well as FEM-literature, for in-depth explanation [2][10][17].

Elasticity

To be able to properly describe a material in a model, one has to be able to describe the material's behavior in response to stimuli. If the scenario being modeled contains thermal as well as mechanical loads, then equations relating the displacement to the increases in temperature and forces need to be established. Basic theory in solid mechanics correlates what is called stresses σ with what is referred to as elastic strains ϵ^e , through

$$\sigma_{ij} = D_{ijkl}\epsilon_{kl}^e \quad (2.9)$$

or inversely as

$$\epsilon_{ij}^e = C_{ijkl}\sigma_{kl} \quad (2.10)$$

if the material is linearly hyper-elastic. The elastic stiffness tensor D_{ijkl} and the elastic flexibility tensor C_{ijkl} have different appearances depending on the material. Eqn. 2.10 can be expressed in matrix format as

$$[\epsilon_{ij}^e] = \begin{bmatrix} \epsilon_{11}^e \\ \epsilon_{22}^e \\ \epsilon_{33}^e \\ 2\epsilon_{12}^e \\ 2\epsilon_{13}^e \\ 2\epsilon_{23}^e \end{bmatrix} = \begin{bmatrix} C_{1111} & C_{1122} & C_{1133} & C_{1112} & C_{1113} & C_{1123} \\ C_{2211} & C_{2222} & C_{2233} & C_{2212} & C_{2213} & C_{2223} \\ C_{3311} & C_{3322} & C_{3333} & C_{3312} & C_{3313} & C_{3323} \\ C_{1211} & C_{1222} & C_{1233} & C_{1212} & C_{1213} & C_{1223} \\ C_{1311} & C_{1322} & C_{1333} & C_{1312} & C_{1313} & C_{1323} \\ C_{2311} & C_{2322} & C_{2333} & C_{2312} & C_{2313} & C_{2323} \end{bmatrix} \begin{bmatrix} \sigma_{11} \\ \sigma_{22} \\ \sigma_{33} \\ \sigma_{12} \\ \sigma_{13} \\ \sigma_{23} \end{bmatrix} \quad (2.11)$$

Different types of material have different microstructure. Assuming orthotropy, Eqn. 2.11 is reduced to

$$\begin{bmatrix} \epsilon_{11}^e \\ \epsilon_{22}^e \\ \epsilon_{33}^e \\ 2\epsilon_{12}^e \\ 2\epsilon_{13}^e \\ 2\epsilon_{23}^e \end{bmatrix} = \begin{bmatrix} C_{1111} & C_{1122} & C_{1133} & 0 & 0 & 0 \\ C_{2211} & C_{2222} & C_{2233} & 0 & 0 & 0 \\ C_{3311} & C_{3322} & C_{3333} & 0 & 0 & 0 \\ 0 & 0 & 0 & C_{1212} & 0 & 0 \\ 0 & 0 & 0 & 0 & C_{1313} & 0 \\ 0 & 0 & 0 & 0 & 0 & C_{2323} \end{bmatrix} \begin{bmatrix} \sigma_{11} \\ \sigma_{22} \\ \sigma_{33} \\ \sigma_{12} \\ \sigma_{13} \\ \sigma_{23} \end{bmatrix} \quad (2.12)$$

which can be re-written using the different elastic moduli E , Poisson's ratios ν and shear moduli G as

$$\begin{bmatrix} \epsilon_{11}^e \\ \epsilon_{22}^e \\ \epsilon_{33}^e \\ 2\epsilon_{12}^e \\ 2\epsilon_{13}^e \\ 2\epsilon_{23}^e \end{bmatrix} = \begin{bmatrix} \frac{1}{E_1} & -\frac{\nu_{21}}{E_2} & -\frac{\nu_{31}}{E_3} & 0 & 0 & 0 \\ -\frac{\nu_{12}}{E_1} & \frac{1}{E_2} & -\frac{\nu_{32}}{E_3} & 0 & 0 & 0 \\ -\frac{\nu_{13}}{E_1} & -\frac{\nu_{23}}{E_2} & \frac{1}{E_3} & 0 & 0 & 0 \\ 0 & 0 & 0 & \frac{1}{G_{12}} & 0 & 0 \\ 0 & 0 & 0 & 0 & \frac{1}{G_{13}} & 0 \\ 0 & 0 & 0 & 0 & 0 & \frac{1}{G_{23}} \end{bmatrix} \begin{bmatrix} \sigma_{11} \\ \sigma_{22} \\ \sigma_{33} \\ \sigma_{12} \\ \sigma_{13} \\ \sigma_{23} \end{bmatrix} \quad (2.13)$$

The elastic properties of both the aluminum and paperboard were defined as orthotropic using the 6×6 matrix in Eqn. 2.13. To then also couple the strains from thermal loading, the total elastic strain can be expanded to include the thermal strain

$$\epsilon_{ij}^0$$

$$\epsilon_{ij}^{e,tot} = \epsilon_{ij}^0 + \epsilon_{ij}^e \quad (2.14)$$

where the contribution of the thermal strains can be re-written as

$$\epsilon_{ij}^o = \alpha_{ij} \Delta T \quad (2.15)$$

where, for an orthotropic material

$$[\alpha_{ij}] = \begin{bmatrix} \alpha_{11} & 0 & 0 \\ 0 & \alpha_{22} & 0 \\ 0 & 0 & \alpha_{33} \end{bmatrix} \quad (2.16)$$

Elastic response of a material is independent of the load history. This implies that if a material is loaded within the elastic region and then unloaded, there will exist no permanent deformation.

Plasticity

If a material is loaded with a large enough load the previously explained models for elastic loading is not sufficient to explain the total strain. During the virtual modeling of this thesis, a plasticity model was needed to determine the mechanical behavior of the aluminum. Technically speaking, when $\sigma > \sigma_y$ plasticity occurs, where σ_y denotes the *yield stress*. Should stresses in the material exceed σ_y , plastic deformations will be introduced in the material and the value of σ_y will be changed, see Fig. 2.6.

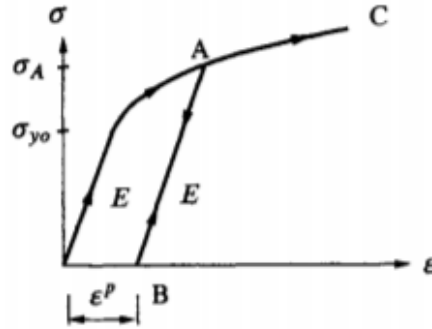


Figure 2.6: Stress-strain diagram of plastic response. If loaded again, the new σ_y is σ_A and permanent deformation ϵ^p has been introduced [17].

The figure shows a load-case where enough stress has been applied to introduce plasticity (σ_{y0}) and illustrates that the unloading from well inside the plasticity zone (A-B) still has the same slope as the elastic loading. ϵ^p are the strains still present after unloading [17]. To analytically manage the introduction of plastic strains, the strain tensor ϵ_{ij} is now defined as

$$\epsilon_{ij} = \epsilon_{ij}^e + \epsilon_{ij}^p \quad (2.17)$$

where ϵ_{ij}^e and ϵ_{ij}^p denote the mechanical elastic and plastic strains respectively. This relation holds for **small** deformations and was used when calibrating the plasticity model in the next chapter. During the virtual simulations, however, **large** deformations were expected, forcing the need of non-linear FEM, described by Krenk [2], as well as an extrapolation of the measured values (see below).

A *yield function* is defined as

$$f(\sigma_{ij}, K_\alpha) = 0 \quad \alpha = 1, 2, \dots \quad (2.18)$$

where K_α are the hardening parameters. These are in turn functions of their internal variables

$$K_\alpha = K_\alpha(\kappa_\beta) \quad \beta = 1, 2, \dots \quad (2.19)$$

This function is defined in such a way that

$$f(\sigma_{ij}, K_\alpha) = \begin{cases} > 0, & \text{not possible} \\ = 0, & \text{when plasticity is developing} \\ < 0, & \text{exhibits elastic properties} \end{cases}$$

The case $f > 0$ does not exist. Instead the *yield surface* is moved, keeping the evolution of plasticity at $f = 0$. Differentiating Eqn. 2.18 and assuming no dependency on time, yields the *consistency condition*

$$\dot{f} = \frac{\partial f}{\partial \sigma_{ij}} \dot{\sigma}_{ij} + \frac{\partial f}{\partial K_\alpha} \dot{K}_\alpha = 0 \quad (2.20)$$

which together with Eqn. 2.19 can be written as

$$\dot{f} = \frac{\partial f}{\partial \sigma_{ij}} \dot{\sigma}_{ij} + \frac{\partial f}{\partial K_\alpha} \frac{\partial K_\alpha}{\partial \kappa_\beta} \dot{\kappa}_\beta = 0 \quad (2.21)$$

The evolving of the internal variables with time can in turn be described as

$$\dot{\kappa}_\beta = \dot{\lambda} k_\beta(\sigma_{ij}, K_\beta) \quad (2.22)$$

where k_β are called evolution functions and $\dot{\lambda}$ is called the plastic multiplier. For orthotropic materials

$$\dot{\lambda} = \dot{\epsilon}_{eff}^p \quad \dot{\epsilon}_{eff}^p = \left(\frac{2}{3} \dot{\epsilon}_{ij}^p \dot{\epsilon}_{ij}^p \right)^{1/2} \quad (2.23)$$

Here $\dot{\epsilon}_{ij}^p$ describes the time-dependent of the yield-surface and is expressed as

$$\dot{\epsilon}_{ij}^p = \dot{\lambda} \frac{\partial g(\sigma_{ij}, K_\alpha)}{\partial \sigma_{ij}} \quad (2.24)$$

where g is a potential function. If *associated plasticity* holds, the potential function is the same as the yield function, i.e. $g=f$. With the use of isotropic hardening

$$\dot{\kappa} = \dot{\epsilon}_{eff}^p \quad (2.25)$$

This makes it possible to re-write Eqn. 2.21 as

$$\dot{f} = \frac{\partial f}{\partial \sigma_{ij}} \dot{\sigma}_{ij} + \frac{\partial f}{\partial K_\alpha} \frac{\partial K_\alpha}{\partial \kappa_\beta} \dot{\kappa} = 0 \quad (2.26)$$

Hill's yield criterion

To be able to adequately describe the properties of rolled aluminum, the Hill yield criterion was adopted and a short discussion on this topic is therefore presented. The initial yield criterion can be formulated as

$$(\sigma_{y0}^2 s_{ij} P_{ijkl} s_{kl})^{1/2} - \sigma_{y0} = 0 \quad (2.27)$$

where isotropic hardening then can be written as

$$f(\sigma_{ij}, K_\alpha) = (\sigma_{y0}^2 s_{ij} P_{ijkl} s_{kl})^{1/2} - \sigma_y = 0 \quad (2.28)$$

s_{ij} is the deviatoric stress tensor and is defined as

$$s_{ij} = \sigma_{ij} - \frac{1}{3} \delta_{ij} \sigma_{kk} \quad (2.29)$$

where δ_{ij} is the Kroneckers delta, defined as

$$\delta_{ij} = \begin{cases} 1, & \text{if } i=j \\ 0, & \text{if } i \neq j \end{cases}$$

$[P_{ijkl}]$ is defined as

$$[P_{ijkl}] = \begin{bmatrix} \tilde{\mathbf{P}} & \mathbf{0} \\ \mathbf{0} & \tilde{\mathbf{Q}} \end{bmatrix} \quad (2.30)$$

where

$$\tilde{\mathbf{P}} = \begin{bmatrix} F + G & -F & -G \\ -F & F + H & -H \\ -G & -H & G + H \end{bmatrix} \quad \tilde{\mathbf{Q}} = \begin{bmatrix} 2L & 0 & 0 \\ 0 & 2M & 0 \\ 0 & 0 & 2N \end{bmatrix} \quad (2.31)$$

F, G, H, L M and N are all material parameters that represent the orthotropy of the material. For the use of this plasticity model during the virtual modeling, these parameters were determined when calibrating the plasticity model at different temperatures. They are defined as

$$\begin{aligned} F &= \frac{1}{2} \left(\frac{1}{R_{22}^2} + \frac{1}{R_{33}^2} - \frac{1}{R_{11}^2} \right) \\ G &= \frac{1}{2} \left(\frac{1}{R_{33}^2} + \frac{1}{R_{11}^2} - \frac{1}{R_{22}^2} \right) \\ H &= \frac{1}{2} \left(\frac{1}{R_{11}^2} + \frac{1}{R_{22}^2} - \frac{1}{R_{33}^2} \right) \\ L &= \frac{3}{2R_{23}^2} \\ M &= \frac{3}{2R_{13}^2} \\ N &= \frac{3}{2R_{12}^2} \end{aligned} \quad (2.32)$$

where R_{ij} are called *anisotropic yield stress ratios*. These values are used as input in Abaqus when defining how the plasticity will evolve [10]. These in turn are defined as

$$\begin{aligned}
R_{11} &= \frac{\bar{\sigma}_{11}}{\sigma^0} \\
R_{22} &= \frac{\bar{\sigma}_{22}}{\sigma^0} \\
R_{33} &= \frac{\bar{\sigma}_{33}}{\sigma^0} \\
R_{12} &= \frac{\bar{\sigma}_{12}}{\tau^0} \quad \text{where} \quad \tau^0 = \frac{\sigma^0}{\sqrt{3}} \\
R_{13} &= \frac{\bar{\sigma}_{13}}{\tau^0} \\
R_{23} &= \frac{\bar{\sigma}_{23}}{\tau^0}
\end{aligned} \tag{2.33}$$

Here $\bar{\sigma}_{ij}$ are the measured yield stress values when σ_{ij} are the only components applied, not equal to zero. The value of σ^0 is defined by the user as the reference yield stress. In a uniaxial tension test

$$[\sigma_{ij}] = \begin{bmatrix} \sigma_{11} & 0 & 0 \\ 0 & 0 & 0 \\ 0 & 0 & 0 \end{bmatrix} \tag{2.34}$$

Eqn. 2.27 would yield

$$\sigma_{yo}\sigma_{11}\sqrt{F+G} = \sigma_y \tag{2.35}$$

Observing the parts of Eqn. 2.28, one can identify

$$\dot{\lambda} \frac{\partial f}{\partial \sigma_{ij}} = \dot{\epsilon}_{ij}^p = \dot{\lambda} \frac{\sigma_{yo}^2}{\sigma_y} P_{ijkl} s_{kl} \quad \frac{\partial f}{\partial K} = -1 \quad \frac{\partial K}{\partial \kappa} = \frac{d\sigma_y(\epsilon_{eff}^p)}{d\epsilon_{eff}^p} \tag{2.36}$$

This together with Eqn. 2.27 and 2.35 yields

$$\dot{\epsilon}_{11}^p = \dot{\lambda} \frac{\sigma_{yo}^2}{\sigma_y} \sigma_{11} (F+G) = \dot{\epsilon}_{eff}^p \sigma_{yo} \sqrt{F+G} \quad \implies \quad \dot{\epsilon}_{eff}^p = \frac{\dot{\epsilon}_{11}^p}{\sigma_{yo} \sqrt{F+G}} \tag{2.37}$$

By plotting the experimental values of σ_{11} and $\dot{\epsilon}_{11}^p$ one can then extract values from the curve $\sigma_y(\epsilon_{eff}^p)$ according to Fig. 2.7 (a) to determine $\frac{\partial f}{\partial K_\alpha} \frac{\partial K_\alpha}{\partial \kappa_\beta}$.

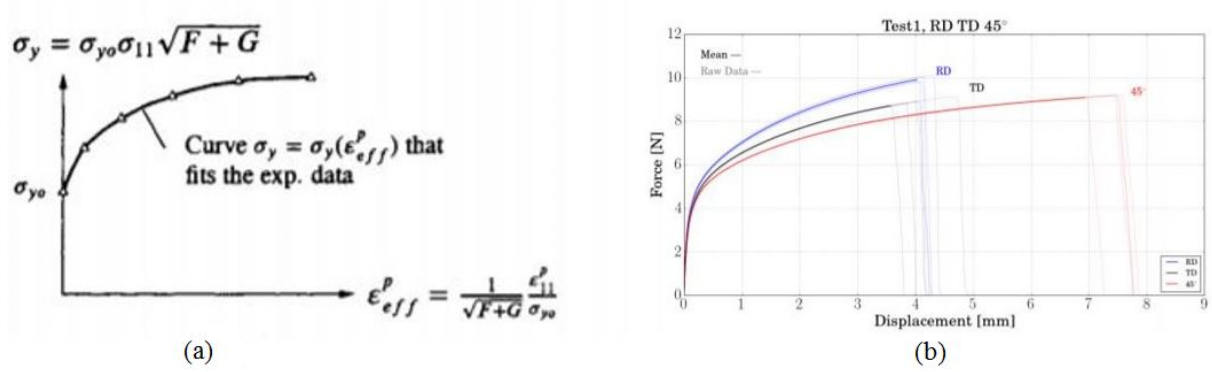


Figure 2.7: The left graph (a) shows a curve used for calibrating a Hill plasticity model [17]. The right graph (b) shows tension tests on aluminum performed by Käck and Malmberg [21].

For large deformations the use of a Ramberg-Osgood expression has been made, to extrapolate the appearance of the unmeasured part of the curve. For a more detailed explanation of this, the reader is referred to *Aluminium foil at multiple length scales, mechanical tests and numerical simulations in Abaqus* by Käck and Malmberg [21]. An example from this thesis regarding the tension testing of aluminum foil can be seen in Fig. 2.7 (b).

Polymer

The material model describing the behavior of the polymer was a time- and temperature-dependent visco-elastic representation. It was constructed using a *parallel network model* consisting of an array of spring/damper components. The model allowed for phase-changes and was possible to use in a large range of temperatures and time-scales.

2.5 Stochastic modeling

When a virtual model is created, ideal conditions are often assumed to preside. In reality, however, boundary conditions, geometries or the material's constituents are rarely "perfect". The stochastic part of a problem formulation can be done in several different ways, e.g. by having different elastic moduli for different elements, different

size of the forces applied or by having irregularities in the geometry. Some examples can be seen in Fig. 2.8.

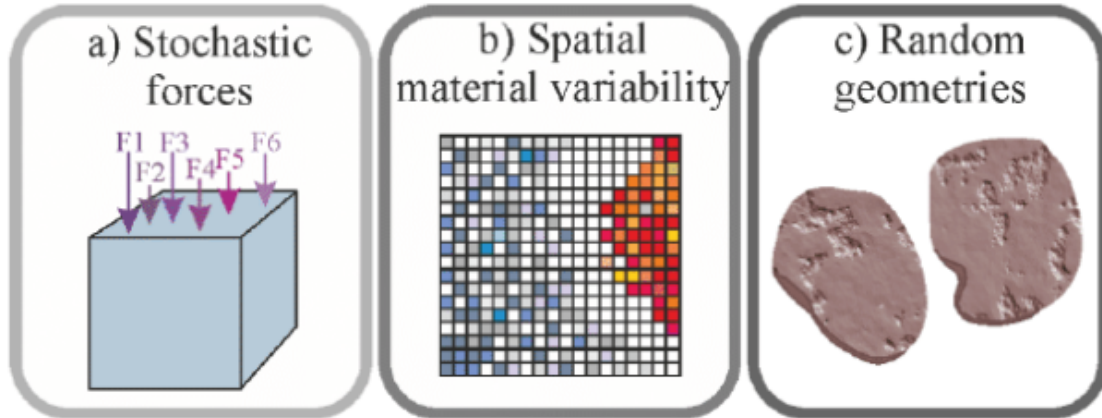


Figure 2.8: Stochastic variables: a) Stochastic forces b) Spatial material variability c) Random geometries [3].

To illustrate the latter, imagine for instance a cubic shell, being compressed along one axis. Would this loading scenario look different if the surface was not perfectly smooth? Would the deformation differ if the shell was thinner along some stretches? To model such occurrences different approaches have been taken, historically. This chapter will introduce the most prominent ones.

Introducing a stochastic component can be useful for simulations in all kinds of areas. In nuclear applications random fields have been used to model the spatial material variability and other defects in nuclear graphite along with other key components of nuclear reactors. This has also been compared with results from simulations of a more deterministic nature. It was found that the material spatial variability increased the magnitude of the von Mises stresses [3].

Monte Carlo-simulations

The most common way of implementing SFEM is by the use of Monte Carlo-simulations. This method combines Monte Carlo-simulations with a regular, deterministic FE-solver. The Monte Carlo-simulation technique basically means using a very large number of values for one or several variables, from a defined probability distribution and running simulations for each of these values, in this case FE-simulations. For instance, assuming that Young's modulus of elasticity would have a normal distribution, several FE-simulations would be run, with values of E varying. The distributions can be defined based on mean values

$$\mu_E \approx \frac{1}{N} \sum_{i=1}^N E_i \tag{2.38}$$

and variance

$$\sigma_E^2 \approx \frac{1}{N-1} \sum_{i=1}^N (E_i - \mu_E)^2 \tag{2.39}$$

where N denotes the size of the sample. Fig. 2.10 illustrates the entire procedure.

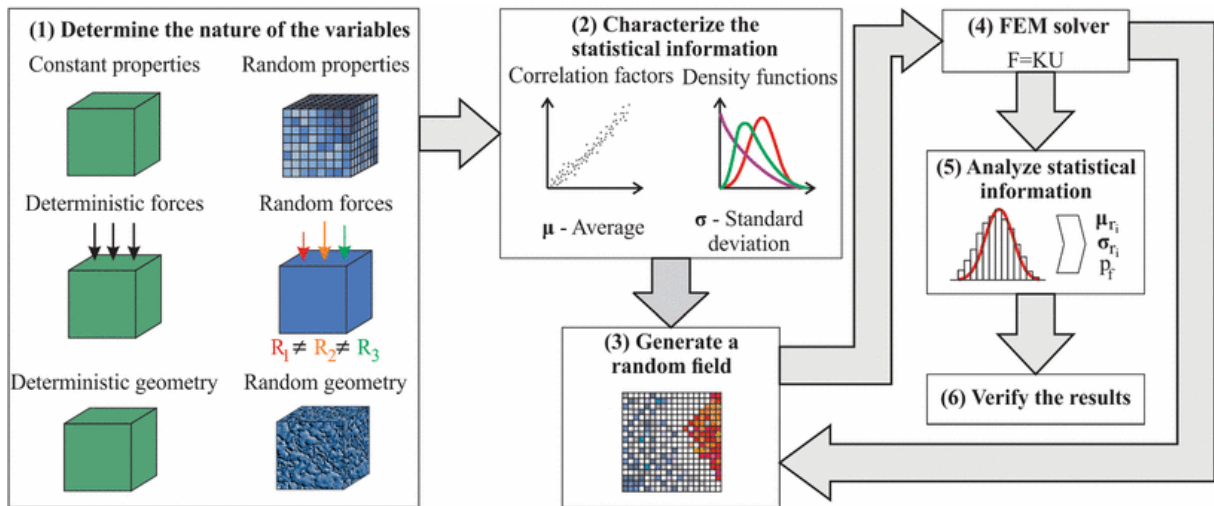


Figure 2.9: The use of Monte Carlo simulations as a stochastic approach [4].

An example of where the geometry of the model was used instead of the material properties, is given by Niemeyer, Schmidt and Wilke. [19].

Perturbation Method

The perturbation method is based on incorporating stochastic expressions directly into the FE-formulation. The external loads, for instance, are set to depend on random variables α_i , where i denotes the number of said variables, and are described using Taylor expansions

$$F = F^0 + \sum_{i=1}^N F_i^I \alpha_i + \frac{1}{2} \sum_{i=1}^N \sum_{j=1}^N F_{ij}^{II} \alpha_i \alpha_j + \dots \quad (2.40)$$

F_i^I and F_{ij}^{II} represent the derivatives

$$F_i^I = \left. \frac{\partial F}{\partial \alpha_i} \right|_{\alpha=0} \quad F_{ij}^{II} = \left. \frac{\partial^2 F}{\partial \alpha_i \partial \alpha_j} \right|_{\alpha=0} \quad (2.41)$$

and F_0 acts as a mean value of the external force vector. Reducing this to a deterministic formulation, the partial derivatives become zero, thus reducing the expression to

$$F = F_0 \quad (2.42)$$

Spectral Stochastic Finite Element Method

The Spectral Stochastic Finite Element Method (SSFEM) focuses mainly of the randomness concerning material parameters. This type of stochastic implementation focuses on decreasing the extensive computational load, often associated with Monte Carlo simulations. The foundation of this method is to utilize *the Karhunen-Loeve expansion* $E(x, \theta)$ of a stochastic process.

$$E(x, \theta) = \bar{E}(x) + \sum_{i=1}^{\infty} \sqrt{\lambda_i(\theta)} \xi_i \psi_i(x) \quad (2.43)$$

where $\bar{E}(x)$ is the mean of the random process, ξ_i is a group of orthogonal random variables, λ_i are the eigenvalues and $\psi_i(x)$ are the corresponding eigenfunctions. This expansion is based on the covariance function C_{EE} of the stochastic process

$$\int_D C_{EE}(x, y) \psi_i(y) dy = \lambda_i \psi_i(x) \quad (2.44)$$

where D is the domain in space to which $E(x, \theta)$ belongs. The eigenfunctions are mutually orthogonal, allowing it to span the space where $E(x, \theta)$ is defined [4][8][20].

3 Method

To be able to create an adequate virtual model, the results from the first virtual models had to be continuously evaluated and compared to physical experiments, as well as scrutinized by XCT. This meant going back and forth between the physical and virtual experiments. The know-how and experience of local engineers as well as members of the Division of Solid Mechanics, was also taken advantage of. Fig. 3.1 illustrates a schematic representation of the workflow and how the validity of the final virtual model was checked using the four most prominent tools. All four of these contributed to perfecting the final model and also had an impact on each other, in a way shown in Fig. 3.1.

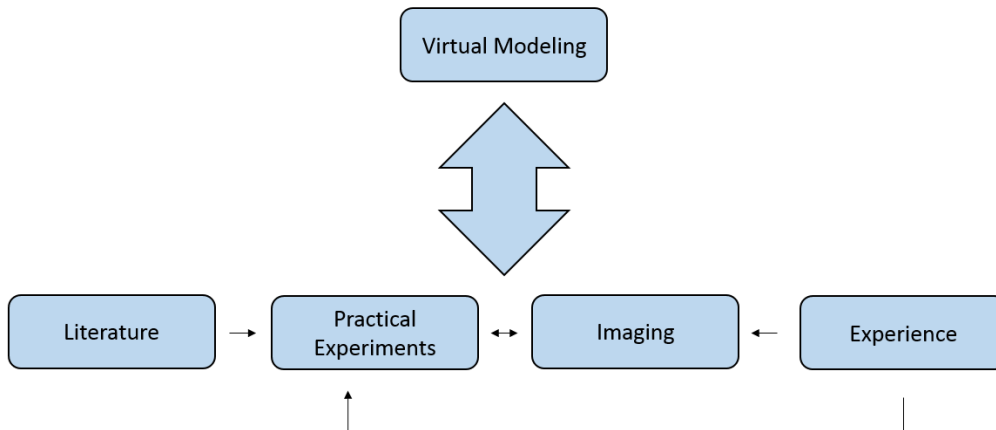


Figure 3.1: Workflow during the thesis.

When conducting the experiments a certain scheme was followed, consisting of *input variables*, a set of parameters that were either labeled *control factors* or *noise factors* and *output variables*. The control factors represented variables that could be controlled in a physical and virtual experiment, such as thermal loading and boundary conditions. The noise factors instead represented factors that were harder to control, but that still could have an impact on the results of the experiments. An example of the latter was the temperature or the humidity of the surroundings. The output was simply defined as what had become of the input, after having been exposed to the noise and control

factors. The process is schematically depicted in Fig. 3.2. This line of reasoning permeated all of the experimenting, both physical and virtual.

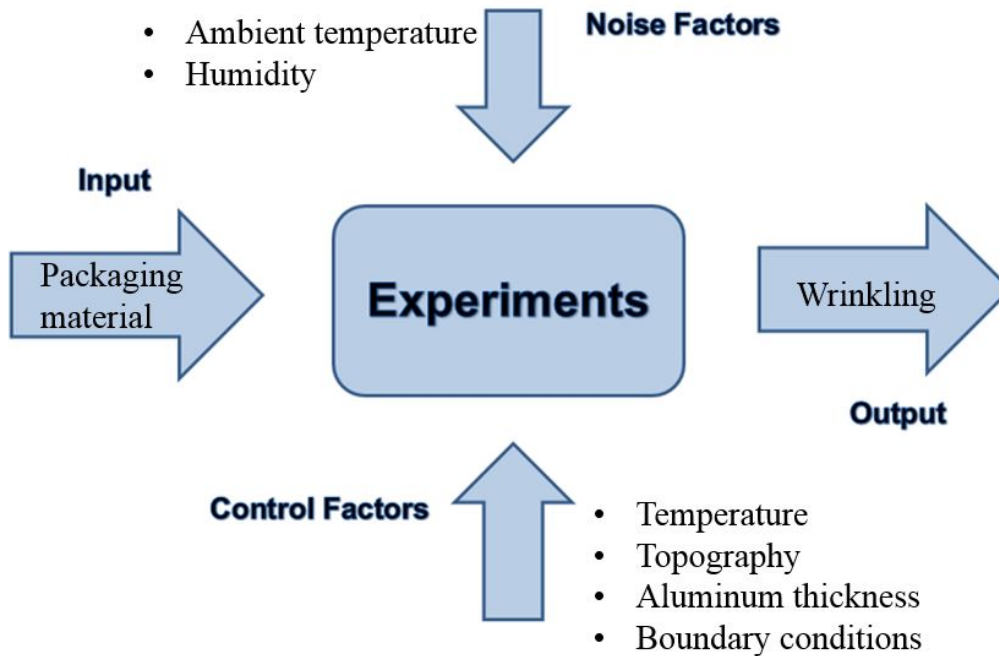


Figure 3.2: P-chart depicting the process.

Physical Experiments

The physical experiments were performed using a heat-gun mounted on a mechanical arm, as well as a heating rig where specific values could be varied with higher precision. Initially a screening procedure was conducted to achieve a greater comprehension of the phenomena involved and to obtain a better understanding of which parameters, and corresponding values, were of interest. After having evaluated this, final experiments were performed only for chosen cases, following the scheme in Fig. 3.2, and only these results were documented. Since the main objective was to understand how underlying stochastic circumstances affect the outcome of a simple loading scenario, no large-scale statistical survey was performed. Rather, single-shot experiments at extreme values were performed, to investigate what brought buckling on. To try to reduce the effect of the noise factors, the samples were stored in rooms with controlled environments as well as climate chambers. The experiments, however, were not per-

formed inside these rooms and how quickly moisture escaped/entered the samples, once removed from the controlled environment, remains unknown.

Virtual Experiments

One of the main goals of this thesis was to create a virtual model, capable of capturing microstructural deviations. This modeling framework may be beneficial to utilize when developing and optimizing filling machine components and to further understand the heating process. In this thesis, the stochastic variation focused upon has been the geometry of the surface of the paperboard, because of the existence of previous work done in that area. Looking closely enough, one will observe that it is far from flat, but rather filled with small hills and valleys, much due to the network of fibers. The virtual model was created in such a way as to reflect these imperfections and was compared to simulations where the interfaces of the different layers of the packaging material was modeled as perfectly flat. This will be described in further detail in Chapter 5.

The virtual model was initially created as a fraction of its desired size, with a relatively coarse mesh. This was done to allow for shorter simulation time. After having decided on a fitting pre-processing procedure, the model was scaled up to match the physical experiments and the procedure in Fig. 3.2 was implemented here as well. Unfortunately, to capture any relevant changes in outcome, the elements had to be very small, increasing the simulation time substantially. This resulted in fewer different scenarios of virtual models, compared to physical ones.

In the early stages of the model, imperfections in the paperboard topography were introduced manually, to see what this would result in. It was, however, desired to obtain a more realistic distribution of voids. To be able to generate such distributions using statistics, large amounts of 2D or 3D data of paperboard topography would have to be collected. The objective of this thesis, however, was to confirm whether irregular geometries gave results different from smooth ones, warranting the creation of such

”geometry-generators”. This constituted the stochastic part of the modeling. The topography of one sample of paperboard was scanned at micrometer level, exported as a mesh and implemented in a FE-model to achieve this. Unfortunately the *Alicona InfiniteFocus*, a 3D micro coordinate measurement machine that can measure surface roughness, used by Filip Larsson when measuring aluminum topography [23], was unavailable due to being broken. This was initially intended to quantify the topography of the paperboard. Instead a microscope of the *Wide-Area 3D Measurement System VR-3000 Series*, with slightly worse precision, was used.

XCT

To obtain a better understanding of what causes the aluminum to buckle, XCT was used before and after thermal loading. The technique enables a full field evaluation methodology. With the use of a 360° scan, a 3D representation of the sample could be obtained [24]. The plan was to compare the images before heating with the corresponding images after heating, to see what could trigger the wrinkling. Since the technique provides images on a micrometer level, the fibers of the paperboard, as well as the air bubbles in the packaging material could be identified. This would enable a more profound understanding of how the excessive heating would alter the geometry and induce permanent deformation.

4 Experiments and measurements

To measure the adequacy of the virtual model, physical experiments using a real model were performed, to allow for comparison between the two. This part also included experiments to reject or validate physical phenomena that could be the cause of the wrinkles. In addition to the physical experiments, XCT was used for validating the results. Imaging before and after heating was performed to allow for observation of the change in microstructure of the sample.

The specimens used for experiments, modeling and XCT had the dimensions $3 \text{ mm} \times 25 \text{ mm}$ (CD \times MD). The width (3 mm along CD) was given its value in accordance with what gave the best resolution in the XCT-scan. The length (25 mm along MD) was arbitrarily chosen with the sole requirement that it should be long enough to allow for one or several wrinkles to arise. The size of the thickness ($\sim 440 \mu\text{m}$ along ZD) was chosen as an approximation of the documented thickness of the different layers.

4.1 Physical experiments

The set-up of the physical experiments were constructed to allow for as simple creation of a virtual experiment as possible. Two different set-ups were used. Initially a proper stationary heating rig was used. Thereafter a self-constructed heat-gun mount was used, to allow for easier virtual model creation.

Heating rig

The heating rig was a stationary platform, used for investigating how altering different parameters would affect the thermal expansion of the packaging material. Parameters such as heating- and cooling-time as well as amount of power, could be altered. This rig induced a current in the aluminum via the physical phenomenon known as *induction*, thereby generating heat.

Experiments

Several sheets of packaging material of much larger size than the aforementioned samples, were heated in this rig. Few experiments were conducted using this rig and the ones that were, were performed using excessive power.

Results

The results differed depending on the power used during the use of induction heating. Using low power created indistinct wrinkles or no wrinkles at all, while using a higher power seemed to make the wrinkles extend longer along the CD direction, as well as to make them more distinct. Ignoring the cases with very low power, which created no wrinkles, the number of wrinkles did not appear to change with increasing power. The wrinkling seemed to occur at evenly distributed intervals.

Analysis

At first, this rig was thought to be the main platform for the physical experiments, the heat-gun being only a mean to do some initial investigation. The way the rig applied heat, however, turned out to be harder to model. It also clamped the samples in an unwanted way, and so this rig remained relatively unused, in fear of not being able to properly replicate its set-up virtually.

This rig was initially also thought to be used to carry out a large-scale statistical survey, to quantify some form of relation between settings on the machine and number of wrinkles. This was rejected, when it became apparent that the number of wrinkles did not appear to depend on the settings possible to alter on the rig. How large they were, however, seemed to depend on the power used. This was not investigated further.

Heat-gun

A heat gun of the model Steinel HL 2305 LCD was used to heat the material, as shown in Fig. 4.1. A heat gun works by emitting a jet of hot air from a rifle-like device. In

these experiments no external technology was used to confirm the temperature of the hot air estimated by the heat-gun itself.



Figure 4.1: Heat-gun of model Steinel HL 2305 LCD used during experiments.

Experiments

The experiments were performed on three different sets of materials.

- First, experiments were performed on a regular packaging material, with a structure like the one described in Chapter 2.1. All different configurations of boundary conditions were investigated.
- Secondly, experiments were conducted on another type of packaging material, where the paperboard had different bending stiffness from the first one. Two different values of the thickness of the aluminum foil were investigated. In this experiments boundary condition configuration (2) was applied.
- Finally, experiments were conducted using a third material, with a higher bending stiffness than the other two. The impact of the position of the layer of clay-coating was to be investigated for two different positions: The default positioning, described in Chapter 2.1, as well as one where the layer of clay were moved to the other side of the paperboard. This change in position would hopefully let the clay fill in the irregularities of the paperboard and result in less

irregular paperboard surface and less wrinkling. In this case boundary condition configuration (2) was applied.

All of the mentioned configurations were thermally loaded with the heat gun with different temperatures according to Table 1-3 for the different materials, respectively. Furthermore, the set-up was composed of the heat-gun held fixed at a distance of ~ 24 mm, with an approximate angle of 90° between heat flow and the surface of the packaging material, as seen in Fig. 4.2.

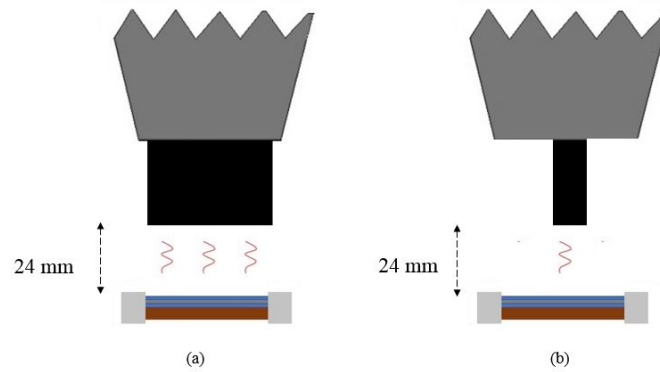
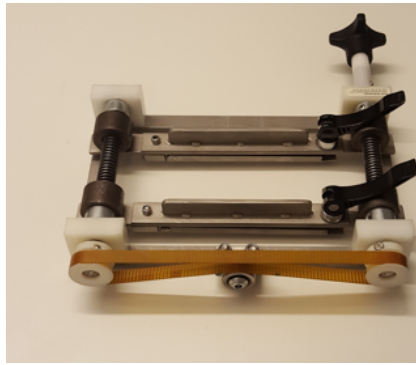


Figure 4.2: Schematic picture of how the heat was applied to the sample with the heat gun. (a) shows the default set-up and (b) shows the use of a focused nozzle.

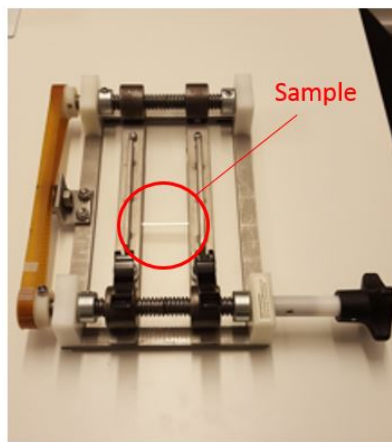
The specimen was clamped at both ends, with the device illustrated in Fig. 4.3.



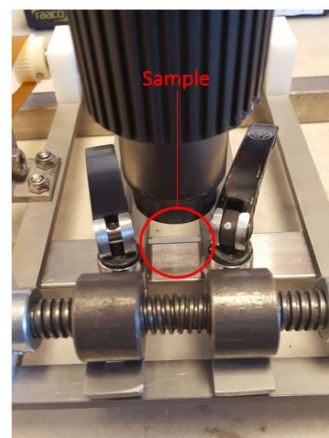
(a) Clamping device used for constraining the samples.



(b) Set-up used during the experiments.



(c) How the samples were clamped.



(d) How the heat was applied.

Figure 4.3: The set-up of the physical experiment.

The heat was applied for 10 seconds. If no wrinkle had occurred by then the specimen was considered unable to buckle. The specimen was $3 \text{ mm} \times 25 \text{ mm}$ and was cut out as shown in Fig. 4.4.

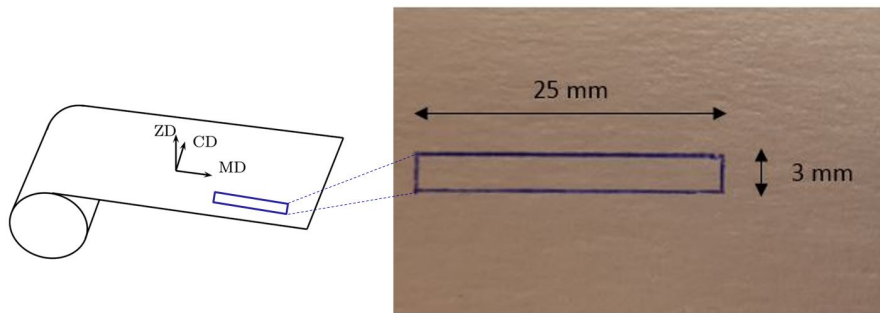


Figure 4.4: The geometry of the sample.

The set-up described above constituted the default set-up. A series of experiments were then conducted using this set-up as reference, but changing one or two parameters at a time. Furthermore, to verify that the phenomenon investigated in this thesis was not the same one as discussed by Askfelt and Ristinmaa [5], four larger pieces of packaging material were exposed to the same thermal loading as the smaller samples. They had the dimensions $60 \text{ mm} \times 70 \text{ mm}$ ($\text{CD} \times \text{MD}$). The heating was applied during 10 seconds. The samples had been stored under different conditions, with respect to temperature (T) and relative humidity (RH). To attain certain levels of humidity and temperature a climate chamber of the model APT.line[®] KBF was used, and is shown in Fig. 4.5.



Figure 4.5: Climate chamber.

The choice of temperature was based on the operating window of the climate chamber, as shown in Fig. 4.6. It was desired to come as close to room-temperature and 0% relative humidity as possible. At room-temperature 23°C , the lowest attainable relative humidity was $\sim 27\%$. At the lowest attainable relative humidity $\sim 10\%$, the temperature had to be set to 40°C . $3\text{ mm} \times 25\text{ mm}$ samples were also stored under these condition to investigate whether these would still exhibit wrinkling.

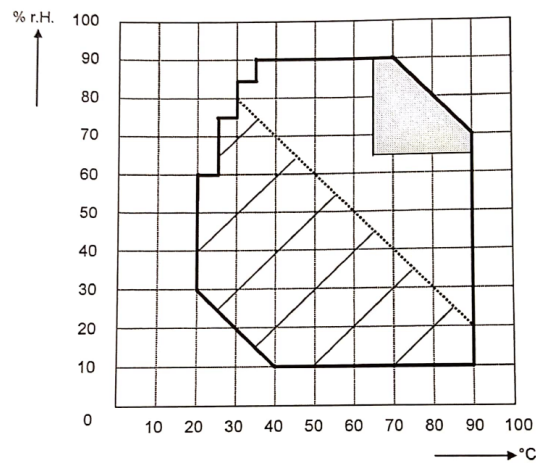
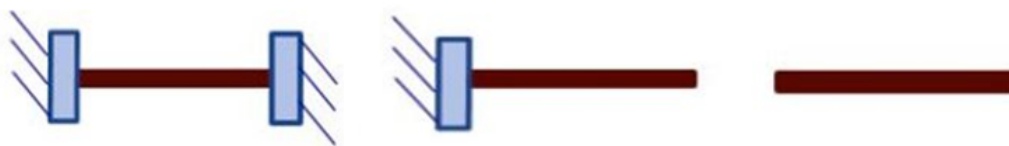


Figure 4.6: The operating window of the climate chamber is shown inside the thicker black line.

Results

The results are presented in the tables below, with the exception of a few special cases. The ✓ means that wrinkling was observed. The 0, 1 and 2 refers to whether it was clamped at 0, 1 or 2 ends, see Fig. 4.7. The clamped end was always the 3 mm long one, i.e. the short end. The values of the temperature refer to the setting of the heat gun.



(a) Clamped at two sides (2). (b) Clamped at one side (1). (c) Not clamped (0).

Figure 4.7: Schematic picture of the different mechanical boundary conditions.

Material 1					
Temperature °C	80	100	120	150	180
BC 0					✓
1					
2		✓	✓	✓	✓

Table 1: A regular packaging material.

Material 2					
Temperature °C	80	90	100	120	180
Thickness 1			✓	✓	✓
Thickness 2				✓	✓

Table 2: A material with two different aluminum thicknesses and BC-configuration (2).

Material 3					
Temperature °C	80	90	100	120	180
Non-reversed			✓	✓	✓
Reversed			✓	✓	✓

Table 3: A material with clay coating on the inside and outside of the paperboard, respectively, and with BC-configuration (2).

Some single-shot experiments were not exposed to the entire range of temperatures. This included exposing a sample to a focused ray of heat. All the different BC configurations were applied. The focusing of the thermal load was achieved by using a metallic nozzle. This loading generated wrinkling using all the different BC configurations.

The results of thermally loading the larger samples are presented in Fig. 4.8. In (a) the sample had been stored in room temperature with an approximate relative humidity of 50 %. After a few seconds wrinkles could be seen. After another couple of seconds the blister was observed [5]. In (b) the sample had instead been stored in a climate chamber with a temperature of 60°C. In this case one wrinkle arose after the same time as in the prior scenario, but without an accompanying blister. In (c) the sample had been stored in 23 °C, with a relative humidity of $\sim 27\%$. In this case multiple wrinkles were visible after the same time as the two other scenarios, with a blister rising after a few seconds longer. In (d) the sample had been stored in 40 °C, with a relative humidity of $\sim 10\%$. In this case multiple wrinkles were visible after the same time as the three other scenarios. A blister was not observed. However, traces of small "blistering tendencies" could be seen at about the same time as blisters had formed during testing on (a) and (c). All the 3 mm \times 25 mm samples that were stored under these conditions exhibited wrinkles.

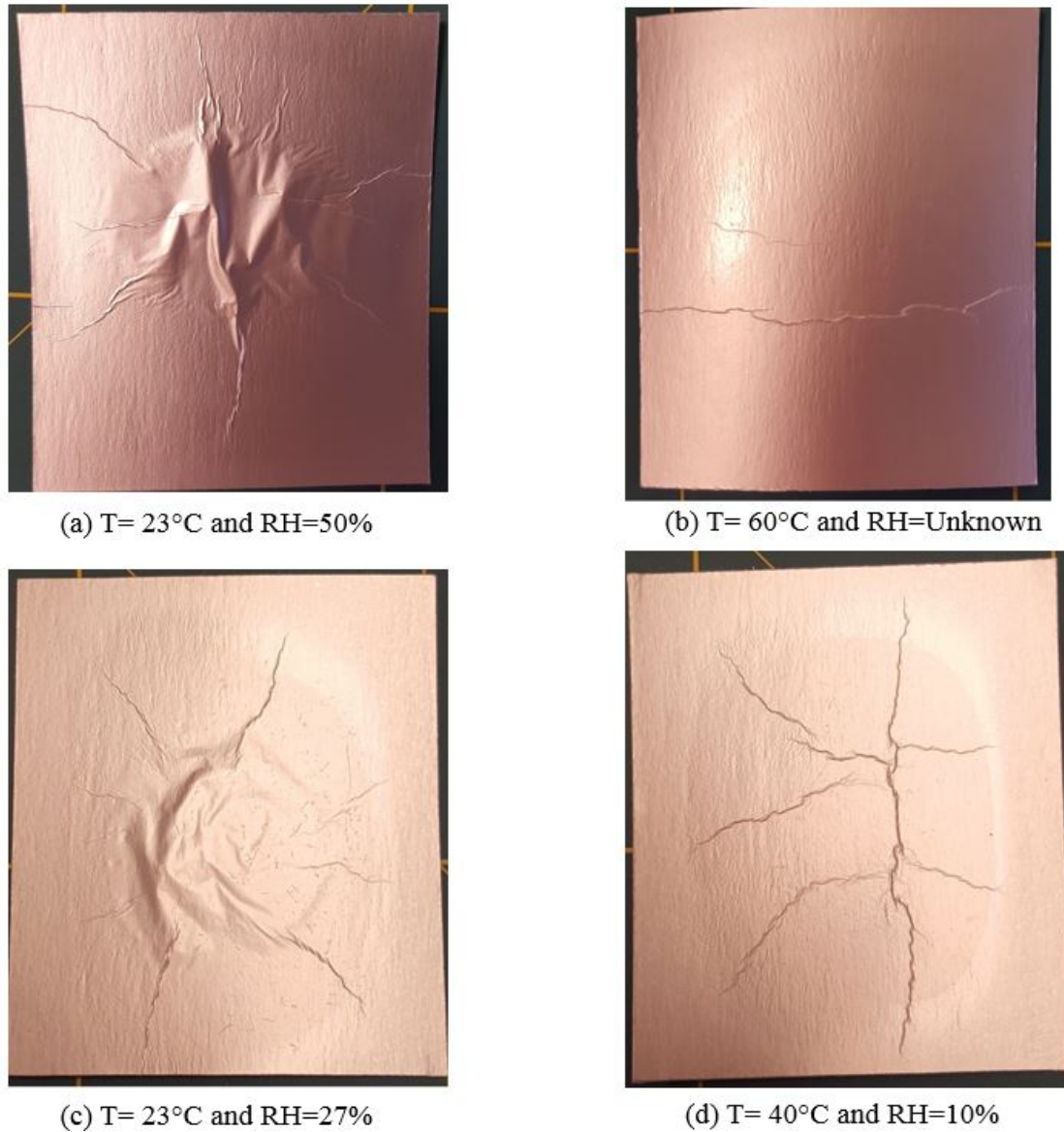


Figure 4.8: The $60\text{ mm} \times 70\text{ mm}$ samples exposed to different temperatures and relative humidities for > 24 hours in a climate chamber.

Analysis

Judging from the results, the best preconditions for a wrinkle to arise seems to be having the sample clamped at both ends and applying a high temperature. By having the sample clamped it is restrained from expanding along the MD-direction, which leads to a deformation in the ZD-direction (buckling). A higher temperature generates a greater expansion of the aluminum foil, which leads to buckling. Insufficient increase

in temperature does not lead to enough expansion of the aluminum foil to generate wrinkles, partly explaining the lack of these when applying lower temperatures. A lower temperature would not yield a polymer fluent enough either, resulting in less movement altogether.

When the packaging material was clamped at one or no sides, wrinkles were only occasionally observed. However, when a focused nozzle was used the specimen seemed to wrinkle every time. It is possible that the difference in temperature between the heated area and the rest of the specimen acted like a boundary condition. This could be explained by polymer expressing more solid qualities outside of the heated area and more fluid qualities inside the heated area, creating a "relative boundary condition". The result of using focused heating should therefore be similar to the result when the sample are clamped at both ends, which it is. It should also be taken into consideration that the temperature setting on the heat gun refers to the heating element, why the temperature is probably higher with the use of a focused nozzle.

When the packaging material was clamped at one end, the other end had no support. This allowed it to bend downwards at this end. The aluminum does not experience as much resistance in expanding along the MD-axis and the stresses, normally causing wrinkles to arise, are not as big.

The thicker layer of aluminum does appear to decrease the wrinkling somewhat, probably owing to the increased bending stiffness.

Changing the position of the clay-coating did not seem to make any difference. This would indicate that the clay is not alone capable of reducing the presence of air bubbles, disturbing the adhesion, to zero.

Regarding the experiments on the larger specimens, shown in Fig 4.8, these results seem to suggest that wrinkling and blistering are two different phenomena occurring

at different times with different physics involved. The wrinkles appear at all tested values of T and RH. The blistering, however, seems to need moisture to be able to arise. This is most likely due to the expansion of water in the paperboard fibers, as it vaporizes. This is reinforced by the results from Ristinmaa and Askfelt's experiments, on what is referred to as "blisters" [5]. To further determine the level of water inside the paperboard *Moisture sorption isotherms for paper and paperboard in food chain conditions* by Parker, Bronlund and Mawson may be consulted [22].

The repeatability of the set-up used during the physical experiments was inadequate. The distance and the angle between specimen and the source of the heat load, as well as the magnitude of the applied load, were manually applied and measured every time, thereby diminishing the precision of the system.

4.2 Image analysis

Tomograph

To be able to further analyze the microstructure of the samples before and after thermal loading, XCT was used. This is a non-destructive technique that allows for visualization of the volume of the sample without invasive procedures. The technology behind this is basically an ordinary X-ray machine, sending high energy radiation through the sample and hitting a detector behind it. Depending on the constituents of the sample, an amount of energy is lost when the radiation attempts to penetrate it. Different elements attenuate radiation at different capacity, thus resulting in different amounts of radiation reaching the detector. This is done while the sample rotates relative to the source and detector. This provides 2D radiographic projections that can be reconstructed, using appropriate software to provide a 3D image of the internal structure of the sample. The machine used was an *Xradia 520 Versa* from the producer Zeiss. This machine implements optical magnification, as well as geometrical magnification to further increase the resolution of the sample [24]. This means putting a microscope behind the sample, as shown in Fig. 4.9. All the scans were performed

in the 4D Imaging Lab at the Division of Solid Mechanics at LTH.

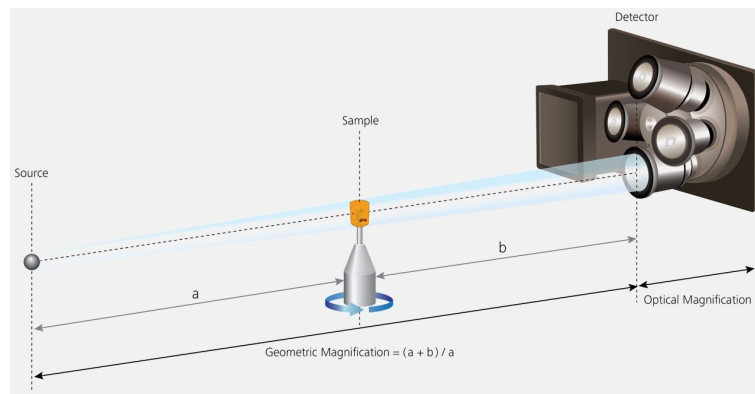


Figure 4.9: Schematic picture of the geometrical magnification in the tomograph [24].

Scanning

The scanned specimen was a 3 mm × 25 mm sample of a packaging material. The small size was needed to get clear pictures in the tomograph. The setup can be seen in Fig. 4.10.

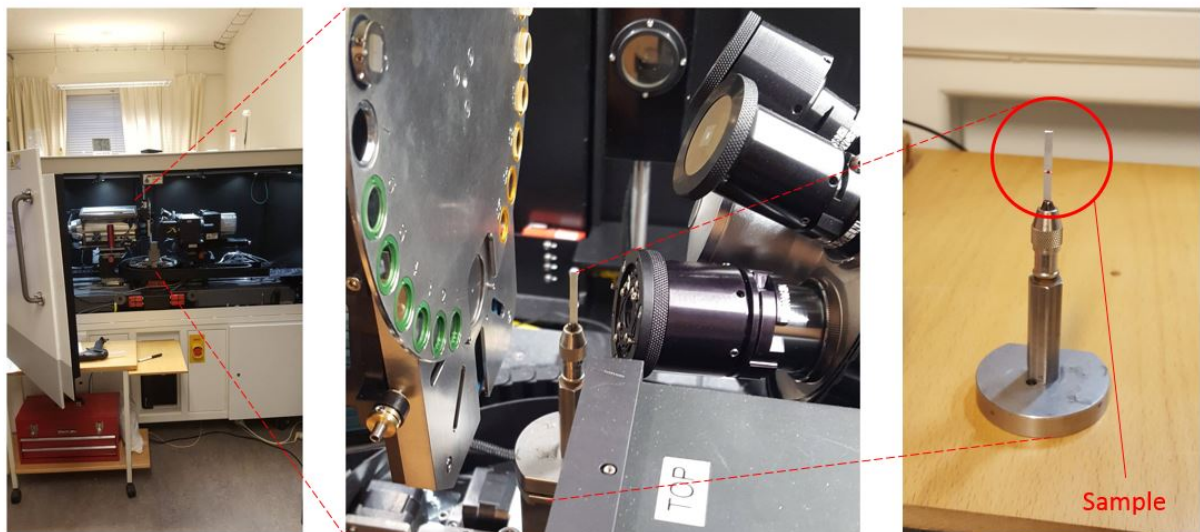


Figure 4.10: The set-up inside the X-ray tomograph.

First, images were produced of the specimen prior to thermal loading. The specimen was then removed from the tomograph and exposed to thermal loading by a heat gun,

while still clamped at one end. The heat was applied through a "window" (Fig 4.11) to produce buckling at the same spot as had been the focus of the first scan, to allow for comparison. The specimen was then put back into the tomograph and new images were produced.

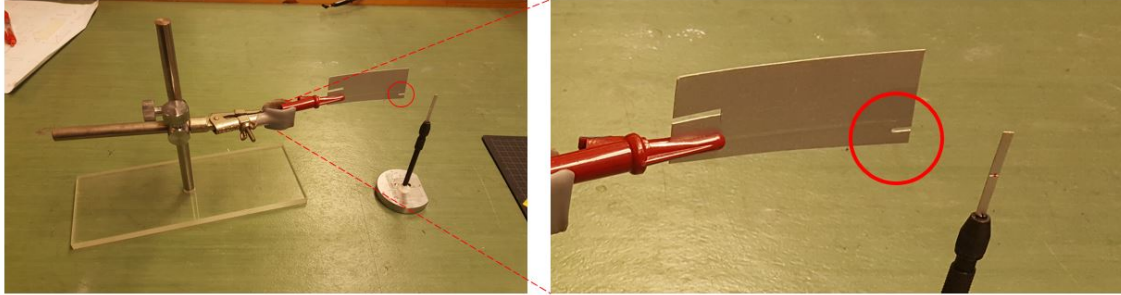


Figure 4.11: The set-up used to heat the sample after the first scan, prior to the second. The red circle shows the "window", through which heat was applied.

Results

The images collected in the XCT-scan were analyzed using the software *Fiji*, an open-source software based on *ImageJ*, but including a set of plug-ins [25]. The images were mainly used to try to quantify and visualize the thickness of the layers and the surface topography, as well as qualitatively illustrate how the heating altered the microstructure of the specimen. To properly illustrate the character of the phenomenon, images were selected from two imaging planes, as well as an image of the entire volume, shown in Fig. 4.12-4.14. Fig. 4.12 shows a cut parallel to the MD-ZD-plane.

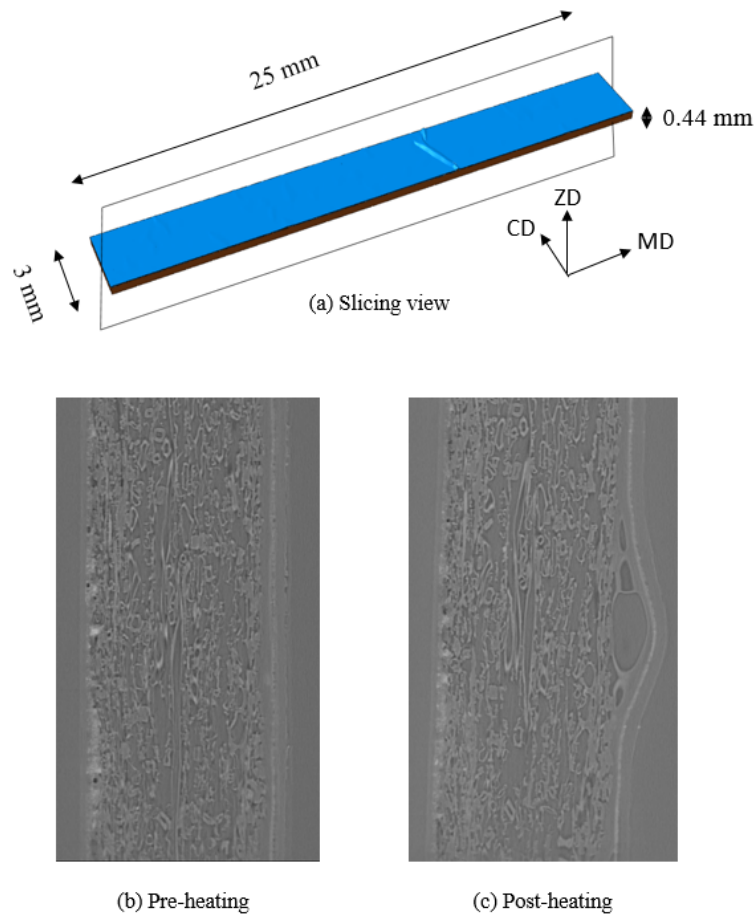


Figure 4.12: XCT-images of packaging material. The cut is performed according to (a). (b) and (c) shows the sample pre- and post-heating, respectively.

The images were also observed in a 3D view, using a plug-in in ImageJ called *Volume Viewer*. Prior to the creation of this the images were filtered using a band-pass filter to get better sharpness of the image. A band-pass filter works by only letting frequencies in a defined interval get through. The 3D view of the filtered images are shown in Fig. 4.13.

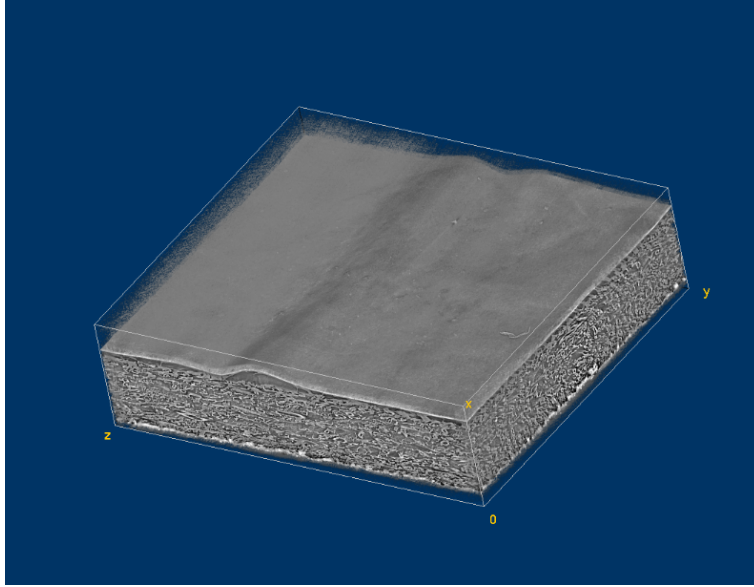


Figure 4.13: A 3D representation of the imaged sample post-heating, where buckling is evident.

Analysis

The plan was to determine the volume of the air-bubbles by calculating the area of the voids showing up in a 2D representation and then adding them to the area in the next slice, calculating the "average area", multiplying it with the distance between two slices (voxel depth) to obtain the volume. For an entire air bubble that would yield

$$V \approx t \left(\frac{A_1 + A_2}{2} + \frac{A_2 + A_3}{2} + \dots + \frac{A_{n-1} + A_n}{2} \right) = t \left(\frac{A_1 + A_n}{2} + \sum_{i=2}^{n-1} A_i \right) \quad (4.1)$$

where V is the volume, t is the voxel length and A_n are the measured size of the area in a slice. Assuming that air is an ideal gas and considering the two states the equation

$$\frac{p_1 V_1}{n_1 R_1 T_1} = \frac{p_2 V_2}{n_2 R_2 T_2} \quad (4.2)$$

holds, where p denotes the pressure, n the amount of substance and R the universal

gas constant. Assuming that no new air enters a bubble and that the temperature of the air before and after corresponds to that of the environment, i.e. 23°C (296.15 K) and 180°C (453.15 K) respectively, Eqn. 4.2 can be rewritten as

$$\frac{p_1 V_1}{T_1} = \frac{p_2 V_2}{T_2} \implies \frac{V_2}{V_1} = \frac{T_2 p_1}{T_1 p_2} \quad (4.3)$$

With the additional assumption that the pressure does not decrease with thermal loading

$$p_1 \leq p_2 \implies \frac{p_1}{p_2} \leq 1 \quad (4.4)$$

one is left with

$$\frac{V_2}{V_1} \leq \frac{T_2}{T_1} \implies \frac{V_2}{V_1} \leq \frac{453.15}{296.15} \approx 1.53 \quad (4.5)$$

as the largest possible expansion of a bubble. Using Eqn. 4.5 and assuming that the bubble can be represented by a sphere, this increase in volume will result in

$$\frac{\frac{4\pi r_2^3}{3}}{\frac{4\pi r_1^3}{3}} = 1.53 \implies \left(\frac{r_2}{r_1}\right)^3 = 1.53 \implies r_2 = 1.15r_1 \quad (4.6)$$

where r_1 and r_2 are the radii before and after heating. Considering the fact that the largest bubbles identified in the pre-heating images have a radius of approximately 33.5 μm , this would be an argument against the expansion of air being the main mechanism behind the phenomenon. According to Eqn. 4.6 above this would only increase the radius of the bubble by approximately 5 μm ; hardly responsible for the buckling seen in Fig. 4.12. If, however, more air were to enter one bubble, by, for instance, letting two or more bubbles coalesce, a larger volume could of course be obtained. This would be analogous to allowing the amount of substance to increase in Eqn. 4.2 above. For this to happen, however, a great enough number of air bubbles would have

to be situated close together. This does not seem to be the case, judging from the images prior to heating. These facts rendered Eqn. 4.1, and the procedure described above it, unused.

The evaporation of the water in the fibers of the paperboard is another subject entirely. As described above, experiments were performed with samples stored at a range of different temperatures and relative humidities. Wrinkles appeared in all these samples, suggesting that the evaporation of water is, at least, not the sole mechanism at work. A more likely explanation to the appearance of the images would be that the tearing of the polymer layer is caused by the buckling of the aluminum foil due to thermal expansion. This buckling seems to nucleate at sites where an air bubble was in the pre-heating state, suggesting that the lack of adhesion causes buckling to occur here. An example of this is seen in Fig. 4.14, where the left slice is taken before and the right slice after thermal loading.

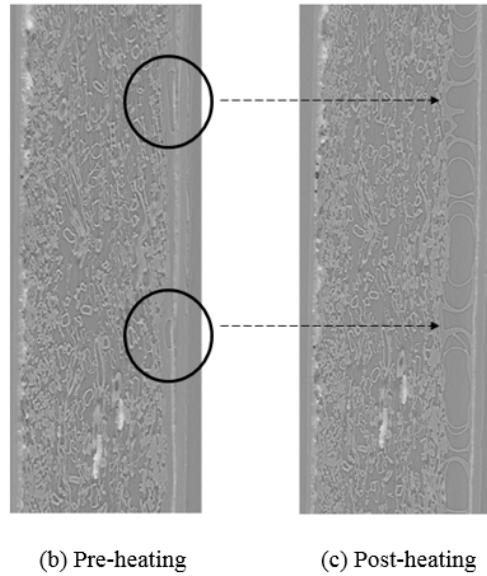
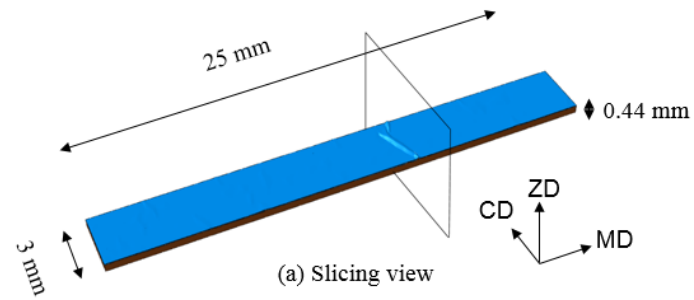


Figure 4.14: XCT-images of packaging material. The cut is performed according to (a). (b) and (c) shows the sample pre- and post-heating, respectively. The arrows shows likely nucleation sites for the buckling due to adhesion failure.

5 Virtual experiments

Parallel to the physical experiments virtual experiments were performed. This procedure was necessary for continued feed-back to validate the adequacy of the model. The model was created using the software HyperMesh, a part of the larger software package HyperWorks [26]. HyperMesh is a pre-processor developed by Altair and is used to create geometries, set boundary conditions, apply loads and do anything related to the model except actually run the simulation. The user creates an input file depending on which solver that is going to be used. In this case the pre-processor was set to create files compatible with the Abaqus explicit solver [27]. HyperMesh was used because of its versatile meshing possibilities. Since actual topography was implemented, it was decided that careful meshing was a key parameter in achieving as realistic results as possible. The process started with the construction of the different layers constituting packaging material and by modeling their inherent properties.

The idea of the virtual experiments was to mimic the physical experiments to an as large extent as possible, but using simulations instead. The same procedure as for the physical experiments was followed, i.e. changing single parameters of a default model, to investigate when the wrinkles appeared. Only the set-up using the heat-gun was modeled virtually, i.e. no induction was modeled. Since no constitutive model existed for the clay-coating, the cases with the reversed board were not modeled.

The *Abaqus explicit solver* was used as solver. The large number of degrees of freedom promoted the use of the explicit solver, due to more efficient memory handling and parallelization capabilities. Moreover, the use of general contact between the aluminum foil and the polymer layer adjacent to the paperboard, along with the fact that excessive local deformation are better handled by the explicit solver, further reinforced this choice [10]. When using the explicit solver in Abaqus the length of a stable time-step is determined by

$$\Delta t_{stable} = \min\left(\frac{L^e}{c_d}\right) \quad \text{where} \quad c_d = \sqrt{\frac{E}{\rho}} \quad (5.1)$$

where L^e is the element length and ρ is the density. To further speed the process up *mass scaling* was used. This meant increasing the density in certain elements to be able to use a larger stable time increment, according to Eqn. 5.1.

5.1 Model

The packaging material was modeled as a 3 mm wide and 25 mm long cuboid, and was divided into layers of paperboard, polymer and aluminum foil, as shown in Figure 5.1.

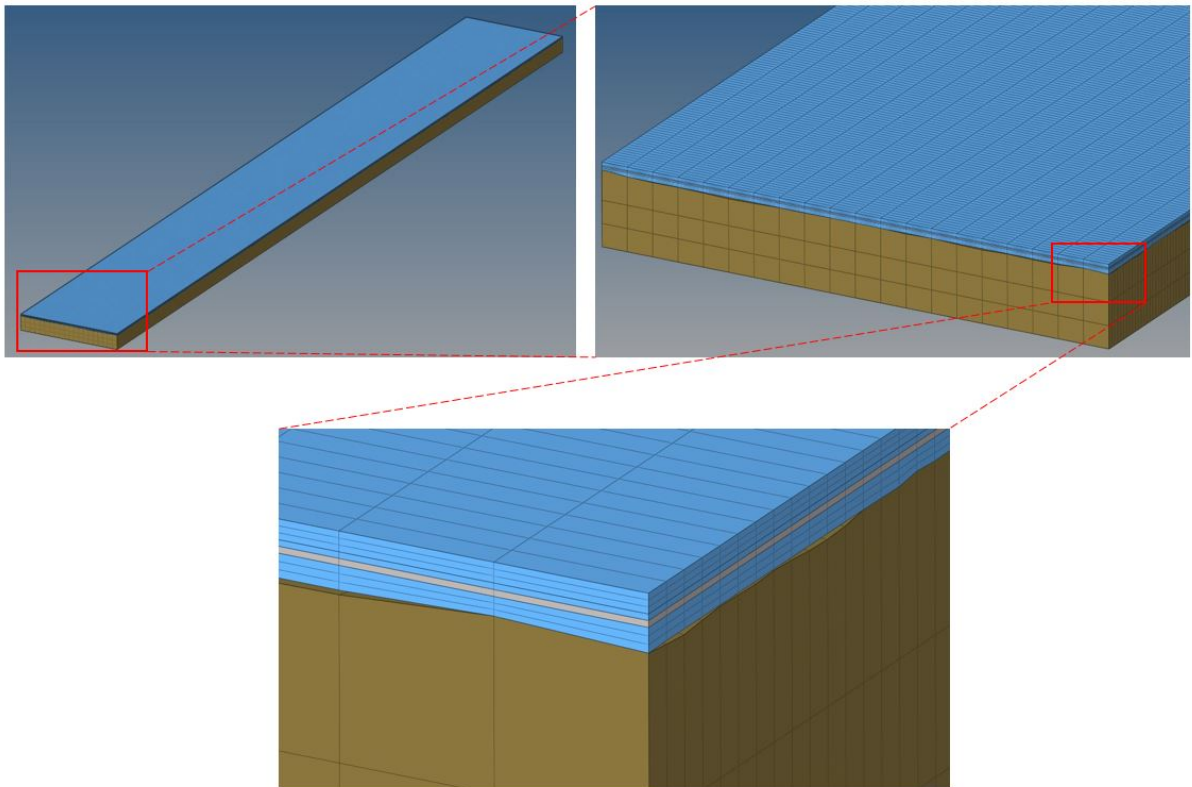


Figure 5.1: The meshed geometry, showing the relative size of the elements. The blue represents polymer, the gray aluminum foil and the brown paperboard.

The mesh consisted of 176 000 hexahedron elements of the type C3D8RT. This type of element was chosen due to the continuum geometry having the shape of a hexahedron and also because of their ability to generate faster simulations than tetrahedrons. The aluminum foil was created as continuum shell elements, whereas the rest was constructed using solid elements. The continuum shell elements were used to allow for the anticipated buckling to occur. This works by introducing three integration points through the thickness of the continuum shell element, while still having only one element layer designed to accurately represent bending.

Because of the relatively big size of the paperboard and the fact that the heat was applied far from this layer, it was meshed with a course mesh, to save simulation time. To avoid having to introduce time-consuming contact-conditions between all the different adjacent layers, elements of different materials shared nodes. General contact between the paperboard and the adjacent polymer was used, meaning that if free surfaces came into contact with each other during the loading, contact would be invoked.

To mimic the experimental setup the default model was assigned the following values during the pre-processing:

- All nodes on the two ends of the model, in the MD-direction, were constrained from movement/rotation in any direction/axis. This represented BC configuration 2 (Fig. 4.7).
- All nodes on the top polymer layer, i.e in the MD-CD-plane, were set to follow the curve profile of the thermal loading (see chapter below). This represented hot air being applied to the top polymer layer.
- All nodes in the entire model were given the initial temperature of approximately 30°C.

The region of interest was mainly the interfaces between the paper-board, the adjacent polymer layer and the aluminum foil and how these would behave when thermal

loading was introduced. The topographical features of the paperboard were the key parameters in the stochastic approach.

In addition to the default model, more models were created to mimic some of the different settings used in the physical experiments. These included models with a variation of heat load, different aluminum thickness and one with a finer mesh, all created with the default model as starting point. The model with a finer mesh was created by dividing each element into five new elements, with equal size, in the CD-direction. Moreover, one model was created with an irregular interface between the polymer layer and the aluminum foil. This setting was simulated due to finding when inspecting the XCT-images.

Curve profile of thermal loading

Due to the simple character of the heat-gun used in the physical experiments, the appearance of the load curve was difficult to determine. The shape finally used was based on previous measurements on packaging material being exposed to hot air. This data was inserted into *Excel* and approximated by a function, using an as high order polynomial as possible [28]. The resulting equation could be expressed as

$$T(t) = 58691t^6 - 135917t^5 + 121165t^4 - 51295t^3 + 9884.9t^2 - 727.19t + 33.681 \quad (5.2)$$

where t is the time and $T(t)$ the temperature. The value

$$R^2 = 0.9938 \quad (5.3)$$

was generated along with Eqn. 5.2, describing how well it approximated the actual data. Due to the character of the thermal amplitude curve creation in HyperMesh, the values during the 0.68 s time interval had to be normalized with respect to the highest value. For this purpose MATLAB was used, see Appendix A1.

Stochastic topography

Introducing a more realistic surface constituted a large part of the stochastic approach and was accomplished in several ways. Initially the layer of paperboard and the adjacent polymer layer were detached from one another. This meant that elements of the different materials that previously shared nodes, were now assigned separate nodes at the same point in space. How these nodes were chosen are described below. As a reference, an "ideal" model was created, with smooth surfaces and no voids present in either interface.

- The first irregular topography was implemented using random alterations of the height of the nodes of the paperboard surface. Nodes of the paperboard elements in the interface between the paperboard and polymer were randomly selected and translated in a direction perpendicular to the polymer layer, towards the rest of the paperboard, see Fig. 5.2. New nodes were then selected and underwent the same procedure. This was done four times. Elements of the paperboard and polymer interface were then allowed to share nodes again, assuming they were sufficiently close together in space ($1 \mu\text{m}$).

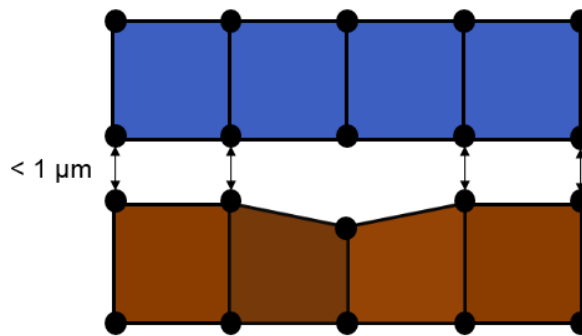


Figure 5.2: Schematic picture of a translated node in the middle of the figure. The rest of the nodes in the interface were merged together.

- The second irregular topography was created by scanning a piece of paperboard with the same dimensions as the model with a microscope of the *Wide-Area 3D Measurement System VR-3000 Series*, shown in Fig. 5.3.

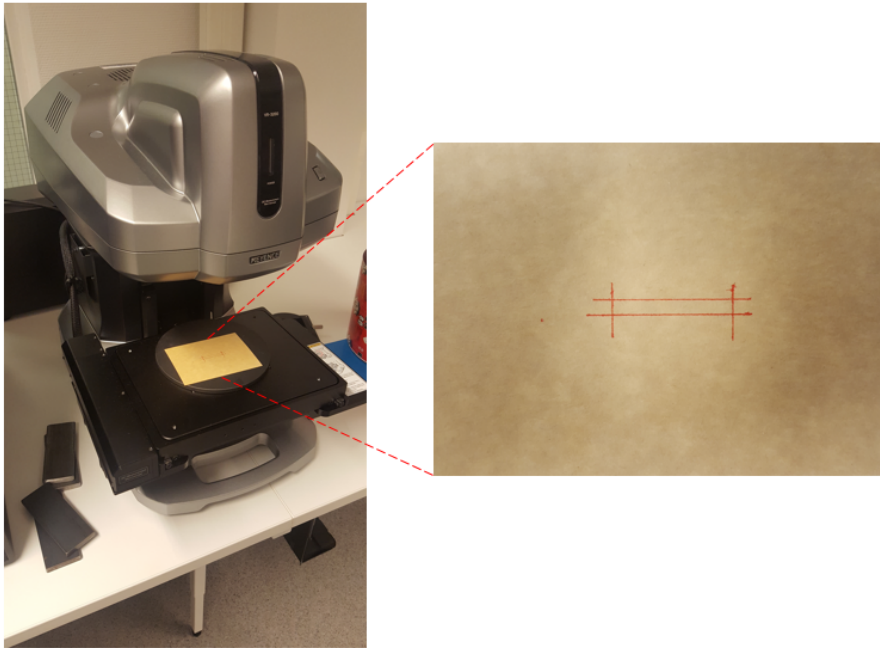


Figure 5.3: Microscope of the *Wide-Area 3D Measurement System VR-3000 Series* used for scanning the topography.

From these scans, a surface topography was extracted and exported in the form of a *stereolithography-file* (.stl-file) shown in Fig. 5.4. Two topographies were scanned. One regular paperboard topography, as well as one where the coating of clay had been placed as described in Chapter 4.1. The latter one was scanned only for visualization purposes and was never implemented in the virtual models.

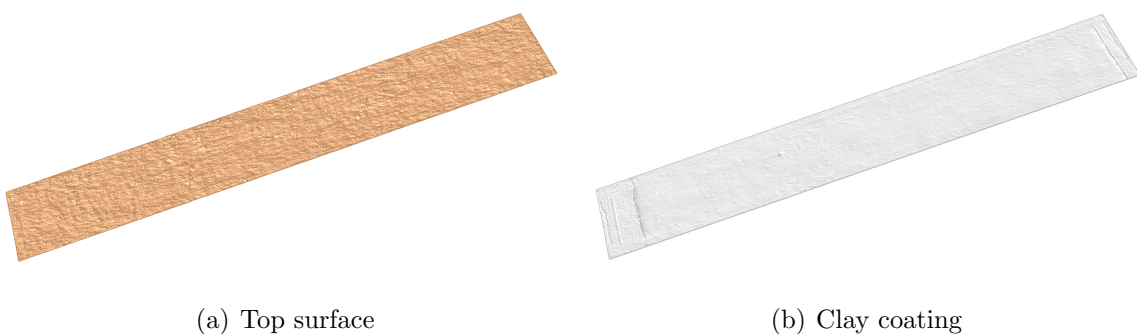


Figure 5.4: (a) The surface of the paperboard (b) The surface of the paperboard with a layer of clay added on top.

The contents of this file were used to manipulate the paperboard elements closest to the polymer. This manipulation consisted of converting the mesh from the .stl-file to a surface and then project the top nodes of the paperboard on to this surface. These operations were performed to convert the triangular mesh from the .stl-file, to a mesh fitting the hexahedral mesh used in the model. When the projection was completed some nodes protruded a lot more than the average node on the surface. Since this concerned about 10 out of 16 000 nodes, it was considered to depend on inaccuracy in the reading of the topography. This was adjusted by calculating the average height from the surrounding nodes and assigning it to the node in question.

To attach the paperboard to the laminate layer a certain procedure was followed, starting with the two layers being completely separated. The paperboard was then translated $1\ \mu\text{m}$ towards the flat laminate surface. The distance between the nodes on the paperboard surface and the corresponding ones on the laminate surface, were measured. If the distance of two nodes was less than $1\ \mu\text{m}$, they were unitized into one node. This procedure was repeated until about half of all the nodes on the paperboard surface had been merged together with a corresponding node on the laminate surface. This yielded a deformed laminate surface with voids present in the paperboard/polymer-interface. This is a realistic set-up, since the laminate will fill some of the holes in the paperboard surface, when the two are pressed together during manufacturing.

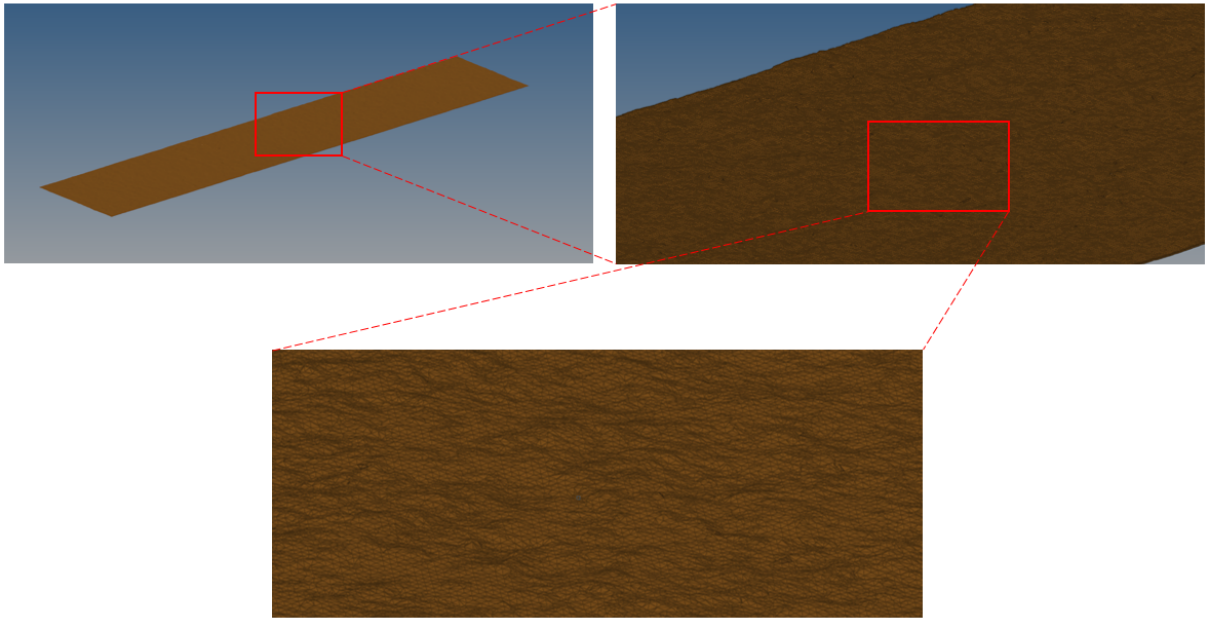


Figure 5.5: The surface mesh produced from the scan.

5.2 Results

In this chapter images of the post-processing are presented. The softwares used to capture the images were HyperView and the Abaqus CAE. For the latter a script was written in the software Python to get repeatability of the positioning and the coloring of the model, see Appendix A Fig. A.2.

The configuration of boundary condition (2) according to Fig. 4.6, heating profile shown in Fig. A.1 (c) (Appendix) with a maximum of 150°C , were considered to be the default settings. These settings were applied to an ideal model where all material layers were smooth and where there were no voids present in the interfaces of the different layers. The result of a 0.68 s simulation of this model is seen in Fig. 5.6.

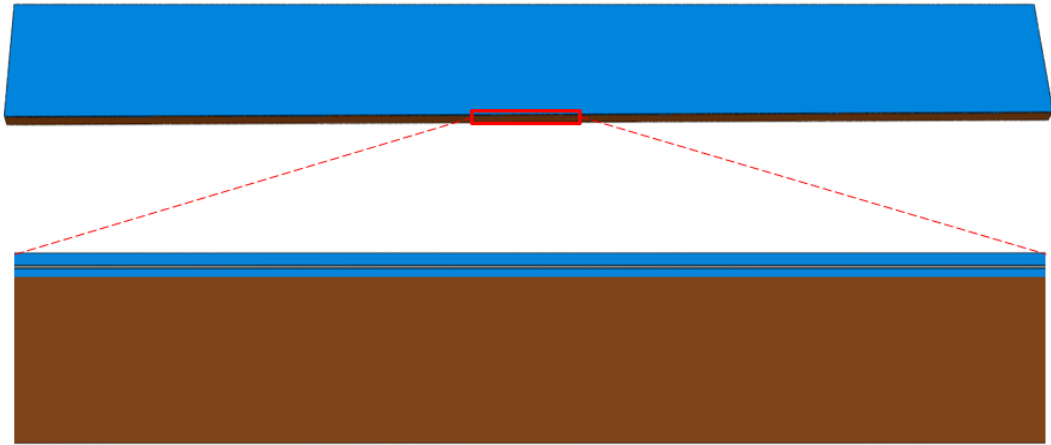


Figure 5.6: The results of a simulation of the ideal model.

Implementing the real topography to the paperboard surface, a simulation was conducted with the same settings as for the ideal model. The results can be seen in Fig. 5.7. This figure illustrates the evolution of a wrinkle, as well as the simultaneous temperature.

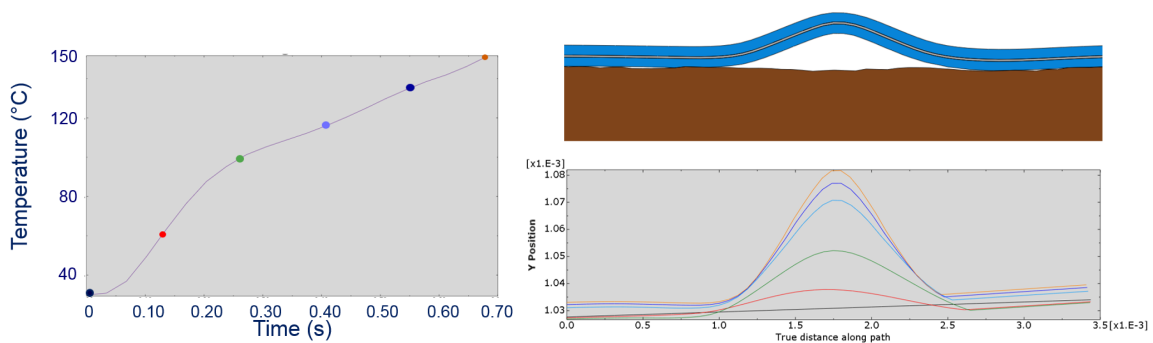


Figure 5.7: (a) shows the temperature of the top nodes w.r.t. time. (b) shows the model at the end of the virtual simulation (upper image) as well as the displacement of the top coordinates of the polymer, with respect to time and temperature, with colors corresponding to the markers in (a).

Fig. 5.8 shows what the simulation looks like from above at the top polymer layer at different moments in time.

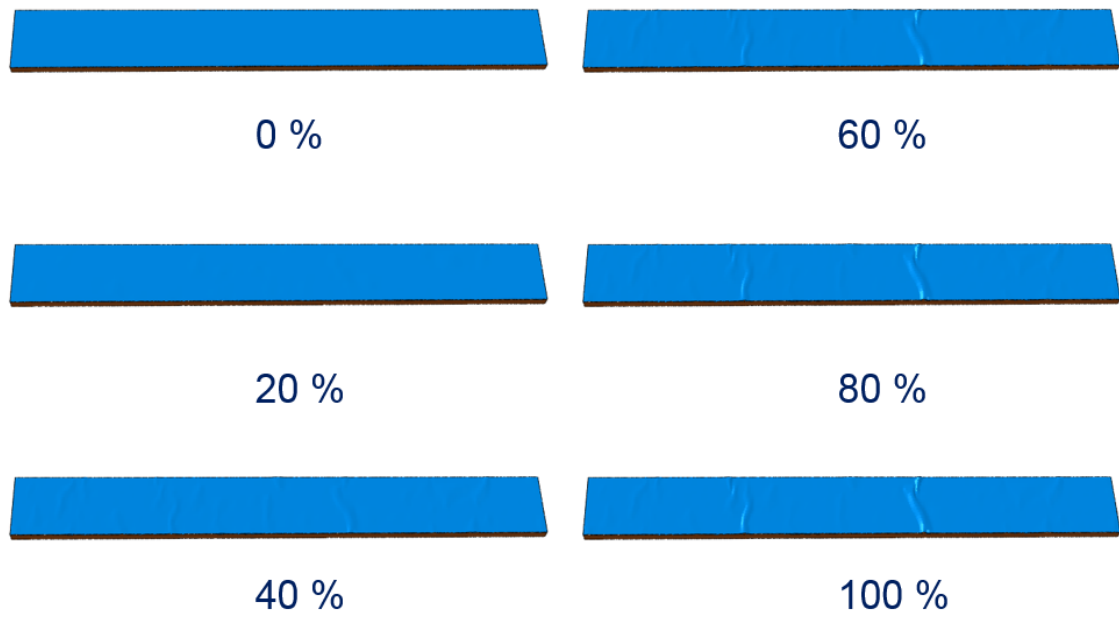


Figure 5.8: The evolution of a wrinkle. Each image is taken at a time expressed in percentage of the total simulation time of 0.68 s.

The stress state of the aluminum foil was investigated for the default model. In Fig. 5.9 the stress field of the aluminum foil can be seen at four consecutive time steps, as the wrinkle evolves.

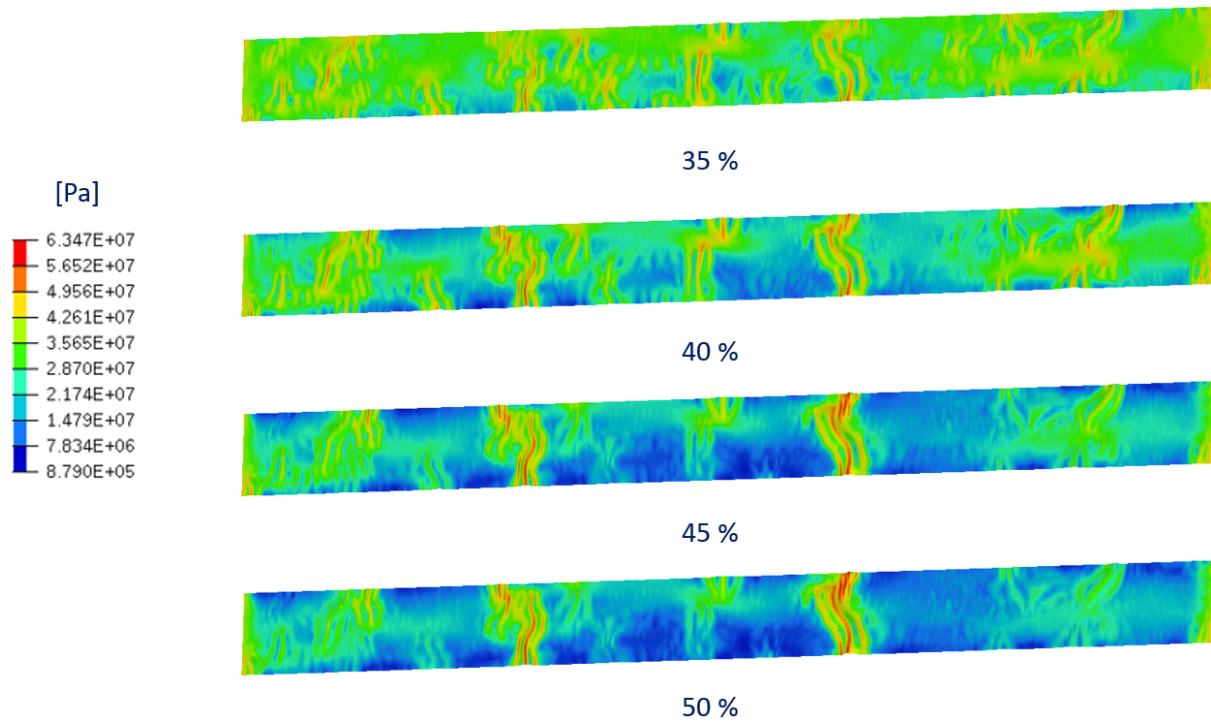


Figure 5.9: The von Mises stress distribution at different times, expressed in percentage of total simulation time.

A model with five times as many elements as the default model, i.e. 880 000, was compared to the default model, see Fig. 5.10. The elements of this mesh were five times as short along the CD-axis.



Figure 5.10: The upper image is the default model after the simulation. The lower image is the result of a simulation of a model with five times as many elements as the default model.

A model with a larger thickness of the aluminum foil was created and simulated with

the remaining settings in accordance with the default model. The result is compared to the default model in Fig. 5.11.



Figure 5.11: The upper image is the default model after the simulation. The lower image is the result of a simulation of a model with thicker aluminum foil.

Not as many experiments were performed using the virtual modeling compared to the real experiments, due to shortage of time. The simulation time of a model was approximately 22 hours.

5.3 Analysis

No obvious wrinkling is present in the model with the ideal interfaces, as opposed to the ones with irregular surfaces, suggesting that models in general could benefit from this type of analysis.

The stress state of the aluminum, illustrated in Fig. 5.8, shows how the stresses increase where the wrinkles arise. The upper image of said figure shows the stress state at the beginning of the wrinkling process. The magnitude of the stress is relatively similar across the surface, but the emergence of small wrinkles can be seen at several positions. When the temperature increases some of the wrinkles grow larger while the others seem to fade out. In the lowest image in Fig. 5.8 only two distinct wrinkles are left. The decrease in the magnitude of the stress in the area around the wrinkles compared with the upper image, suggests that only a limited amount of

wrinkles can be expected depending on the size of the specimen.

Since mass scaling was used it was of importance to investigate whether this affected the results of the simulations. To ensure that the increase in weight, due to mass scaling, did not affect the likelihood of the results, the kinetic energy and strain energy were plotted with respect to time (Fig. 5.12). This comparison is relevant at the time of the wrinkling, i.e. approximately 0.25 s into the simulation. In Fig. 5.12 the kinetic energy seems to be sufficiently small, in comparison to the strain energy, 0.25 s into the simulation, to be ignored.

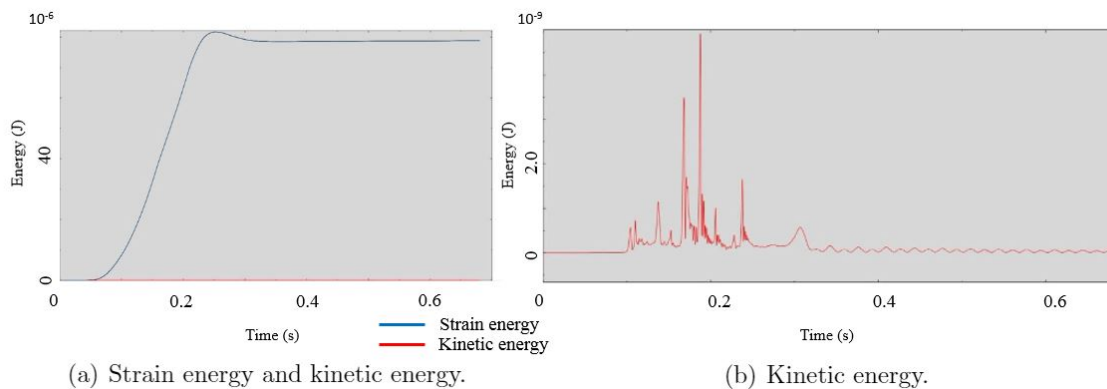


Figure 5.12: (a) shows both the strain and kinetic energy, while (b) shows only the kinetic energy.

A model with a five times finer mesh than the default model was simulated and the result was compared to the result of the default model, see Fig. 5.10. Without changing any other settings, the results of the two models differ. With a finer mesh the smaller wrinkle on the left side of the specimen vanishes and the right wrinkle becomes more distinct. This suggests that the mesh of the default model was too coarse. However, the simulation time of the default model was 22 hours while it was 110 hours for the model with a finer mesh. A simulation time of this magnitude is very time-consuming, especially if more than one parameter is to be tested.

The model with thicker aluminum foil was compared to the default model in Fig.

5.11. In this figure the model with a thicker aluminum foil only shows a wrinkle at one position, similar to what the model with a fine mesh did. This could be due to the elevated bending stiffness of the foil.

A change of the stochastic geometry to include the interface of the aluminum foil and the laminate layer, instead of the interface of paperboard and laminate, was also investigated. The results from this simulation were similar to the results of the default model, why no deeper analysis of this result was carried out.

6 Comparison and Conclusion

Comparison between physical and virtual experiments

The XCT images from post-heating were compared to the results of the virtual experiments. When the two different types of experiments were compared, several things were distinguishable. Using the default settings, i.e. clamping at both ends and applying heat according to Fig. 4.2, yielded similar results for physical and virtual experiments. Fig. 6.1 illustrates this with a virtual image and an XCT-image next to each other. The specimen from the XCT-scan was, however, not the same as the one scanned by the Wide-Area 3D Measurement System microscope. The two images should therefore not look exactly the same, but merely show similar qualities.

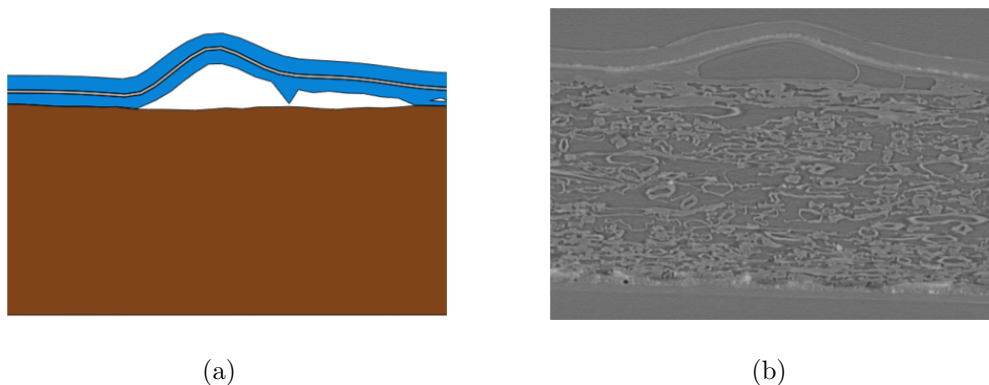


Figure 6.1: (a) Cross-section of the default model at the end of the simulation.
(b) XCT-image of packaging material after thermal loading.

Judging from this, the virtual experiments seem to have captured the shape of the wrinkle and its size as well. The slices are cut perpendicular to the wrinkle, parallel to the MD-ZD-plane. During the physical testing (Tables in Chapter 4) sizable changes were observed somewhere between 80°C and 100°C. In the model, however, these corresponding changes seemed to take place somewhere between 100°C and 120°C, as is illustrated in Fig. 6.2. The time difference between the two needs to be taken into consideration. The physical experiments were performed during 10 seconds while the virtual model had a simulation time of 0.68 seconds. It is reasonable to believe that the extra time increases the chance for a wrinkle to arise. If the model had been

simulated for 10 seconds instead it is possible that the wrinkling had occurred at lower temperatures than the interval between 100°C and 120°C.

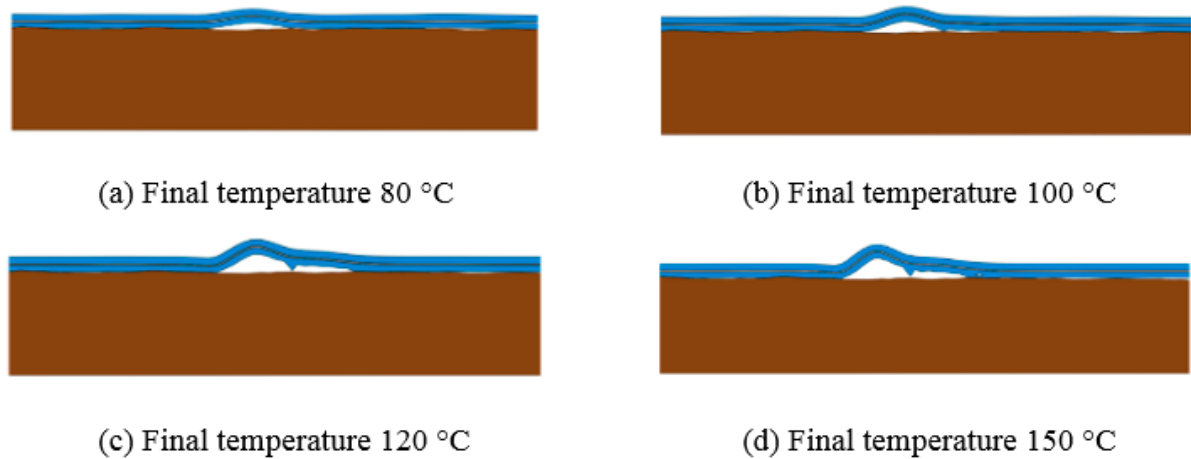


Figure 6.2: Images of cross-sections at the end of four simulations. The load-curve looked the same for all of them, but were scaled according to their respective maximum temperature.

Choosing different configurations of boundary conditions seemed to have a large impact on the physical experiments (Table 4.1), and the corresponding virtual representations showed similar tendencies. In the simulations, when clamped at only one end, there seemed to be less wrinkles overall. However, individual wrinkles could actually be even larger than its clamped-at-both-ends counterpart. Since there were no visible wrinkles at all during the physical experiments, when loading with only one end clamped, this suggest an incomplete model or experimental set-up.

In the physical experiments the thickness of the aluminum foil affected the temperature needed for the wrinkling to occur. However, in the virtual experiments the wrinkles occurred at approximately the same temperature, but the number of wrinkles was decreased to one.

Conclusion

Observing the results of the physical and virtual experiments along with the XCT, there is a definite difference between using a perfectly smooth paperboard surface and an irregular one. Scanning the topography of every single sheet of paperboard ever being virtually modeled is of course impossible. However, if possible to *generate* similar irregular surfaces based on a large number of statistical data, these would be able to act as the inherent randomness of a stochastic system and microstructural phenomena would be captured. The results of the experiments of this thesis suggest that there might exist an optimal temperature for heating packaging material. This could potentially be used to further investigate how to optimize filling machine parameters.

Additional conclusions are presented below:

- Using a multidisciplinary approach, see Fig. 3.1, proved fruitful in understanding and modeling the physics involved in generating the wrinkles. Further investigation would most likely benefit from continuing on this track.
- XCT can be used to capture the microstructural phenomenon wrinkling. Visualization along different cuts allows for a more complete understanding of the expansion of the wrinkle. The scrutiny of the images was mainly qualitative in nature and could perhaps benefit from additional quantitative inspection.
- The mechanical boundary conditions and the temperature play a large part in causing as small samples as was used in this thesis, to wrinkle. Also the thickness of the aluminum foil as well as the size of the area of the nozzle in relation to the size of the sample, seem to be of importance.
- The wrinkling phenomenon seem to be caused by buckling of the aluminum foil. This is in turn caused by thermal expansion of the aluminum in combination with the extensive range of viscosity of the polymer. However, from the experiments performed, it is not possible to completely rule out the effect of moisture.

- The virtual model constructed can capture the wrinkles seen in the physical experiments. However, it does not seem to behave similar to reality in all different cases simulated, suggesting room for improvement or simply the need of more exact physical experiments.

- The stochastic part of this thesis consisted of displacing nodes at random, as well as implementing readings from a measuring device to simulate real surface structure. Creating software that could virtually generate this surface structure through algorithms would simplify the process and complete the stochastic approach. The resulting geometries would not, of course, be an exact representation, but would save time and hopefully produce results realistic enough to capture phenomena such as buckling.
- Improve the experimental set-up to include more exact measurements. For example, the heat-profile used in the model was taken from previous measurements used in a different context, whereas the true heating profile for the physical experiments remains unknown. A proper rig, with more controlled repeatability, as well as the possibility of changing parameters more easily, would give more precise results. An attempt at the construction of such a rig, based on an industrial robot, was made, during the progression of the thesis, but proved too time-consuming.
- Perform XCT imaging before and after thermal loading of a dried-out sample, to observe whether the results are similar to what was observed when using room-temperature and ambient humidity. If it is, this would further strengthen the proposition that water vapor is not, at least, alone in provoking the initial buckling.
- Investigate how larger models would handle this level of refinement of their surface structure and optimize mass scaling, as well as element size in the different material layers. For these simulations to be useful, the computational time should not be too long.
- Investigate the thermal properties of the aluminum foil properly, to determine its thermal expansion along different material axes.
- Perform in-situ heating using XCT to characterize the mechanisms governing the phenomena.

- When fusing the paperboard topography with the polymer, future works could base the distance between the two layers on actual measurements, rather than on arbitrary approximations.

References

- [1] Tetra Pak, *Tetra Pak i korthet* [Internet], [cited 2017 Sep 7] Available from: <http://www.tetrapak.com/se/about/tetra-pak-in-brief>
- [2] Krenk S. *The analysis of non-linear solids and structures*. Cambridge: Cambridge University Press; 2009.
- [3] Mena Arregui J D , Margetts L, Evans LI M, Griffiths D V, Shreerlikht A, Cebamanos L, et al. *The Stochastic Finite Element Method for Nuclear Applications*. Conference paper: ECCOMAS Congress. 2016.
- [4] Arregui-Mena J D, Margetts L, Mummery P M. *Practical Application of the Stochastic Finite Element Method*. Archives of Computational Methods in Engineering. 2016 March;23(1):171-190.
- [5] Askfelt H, Ristinmaa M. *Experimental and numerical analysis of adhesion failure in moist packaging material during excessive heating*. International Journal of Heat and Mass Transfer. 2017 Jan;31(108 part B):2566-2580.
- [6] Im S H, Huang R. *Evolution of Wrinkles in Elastic-Viscoelastic Bilayer Thin Films*. Journal of Applied Mechanics. 2005 Nov;72(6):955-961.
- [7] Tetra Pak, *Förpackningsmaterial* [Internet], [cited 2018 Jan 3] Available from: <https://www.tetrapak.com/se/packaging/materials>
- [8] Sparr A, Sparr G. *Kontinuerliga system*. 2 ed. Lund: Studentlitteratur AB; 2010.
- [9] Wikström Frank. *Funktionsteori*. 1 ed. Lund: Studentlitteratur AB; 2014.
- [10] Dassault Systèmes. *Abaqus Users Manual*. 2017.
- [11] FEniCS Project. *Solving PDES in Python - the Fenics tutorial volume I* [Internet]. [cited 2017 Nov 02]. Available from: <https://fenicsproject.org/pub/tutorial/html/..ftut1006.html>

- [12] Ljung C, Saabye Ottosen N, Ristinmaa M. *Introduktion till hållfasthetslära-Enaxliga tillstånd*. Edition 1:3. Lund: Studentlitteratur AB; 2007.
- [13] Trafikverket. *Solkurvor på järnvägen* [Internet]. Borlänge: Trafikverket; 2015. [cited 2017 Oct 19]
Available from: <https://www.trafikverket.se/om-oss/nyheter/redaktionella-sidor/solkurvor-pa-jarnvagen/>, accessed October 19th
- [14] Wikiwand. *Ductility (Earth science)* [Internet]. [cited 2018 Jan 8] Available from: [http://www.wikiwand.com/en/Ductility_\(Earth_science\)](http://www.wikiwand.com/en/Ductility_(Earth_science)), accessed January 8th 2018
- [15] Khattak O. *Folding: Mechanisms and processes*. 2015 August [cited 2017 Oct 23] In: Learning Geology [Blog on the internet]. Owais Khattak; 2015. Available from: <http://geologylearn.blogspot.se/2015/08/folding-mechanisms-and-processes.html>, accessed October 23rd
- [16] Xue X L, Wang S B, Jia H K, Li L A, He W. *Experimental Investigation on buckling of Thin Films in Mechanical-Thermal Coupled-Field* Physics Procedia. 2011;19:158-163
- [17] Saabye Ottosen N, Ristinmaa M. *The Mechanics of Constitutive Modeling*. Elsevier Science Limited; 2005.
- [18] Borgqvist E, Tryding J. *PhD Paper Mechanics Course Seminar*. 2017 Aug.
- [19] Niemeyer F, Schmidt H, Wilke H. *Geometry strongly influences the response of numerical models of the lumbar spineA probabilistic finite element analysis*. Journal of Biomechanics. 2012 May;45(8):1414-1423.
- [20] Ghanema R G, Kruger R M. *Numerical solution of spectral stochastic finite element systems*. Computer Methods in Applied Mechanics and Engineering. 1996 Jan;129(3):289-303.

- [21] Malmberg C, Käck B. *Aluminium foil at multiple length scales, mechanical tests and numerical simulations in Abaqus*. Lund: LTH; 2015 [cited 8 Jan 2018]. Available from: <https://lup.lub.lu.se/student-papers/search/publication/7451137>
- [22] Parker M E, Bronlund J E, Mawson A J. *Moisture sorption isotherms for paper and paperboard in food chain conditions*. Packag. Technol. Sci. 2006;19(4):193-209.
- [23] Larsson F. *Surface topography measurements of thin aluminium foil transferred to FE-simulations*. Lund: LTH; 2016 [cited 8 Jan 2018]. Available from: <https://lup.lub.lu.se/student-papers/search/publication/8883739>
- [24] Zeiss. ZEISS Xradia 520 Versa [Internet]. Germany: ZEISS. [cited 2017 Nov 2]. Available from: <https://www.zeiss.com/microscopy/int/products/x-ray-microscopy/zeiss-xradia-520-versa.html>
- [25] Fiji. (*Fiji is just*) *ImageJ*, ver. 2.35. [computer program]. Available from : <https://fiji.sc/>.
- [26] Altair. *HyperWorks*, ver. 2017.2 [computer program]. Altair; 2017.
- [27] Dassault Systèmes. *Abaqus/CAE*, ver. 2017 [computer program]. Dassault Systèmes; 2016.
- [28] Microsoft. *Excel*, ver. 2016 [computer program]. Microsoft Office; 2016.
- [29] Hallbäck N, Korin C, Barbier C, Nygård M. *Finite Element Analysis of Hot Melt Adhesive Joints in Carton Board*. Packag. Technol. Sci. 2014;27(9):701-712.

A Appendix

```

clc
clear all

% Time vector in seconds
time=[0:0.001:0.68];

% Polynomial approximation of temperature data
temp=58691.*time.^6-135917*temp.^5+121165.*temp.^4-51235.*temp.^3+9884.9.*temp.^2-
+33.681;

% Normalized vector of temperature values
temp_scale=temp/temp(681);

% Plotting the polynomial w.r.t. time
plot(time,temp_scale)

% Labeling the axes
xlabel('time (s)')
ylabel('Normalized temperature')

% The size of a step
discrete_step=1/13;

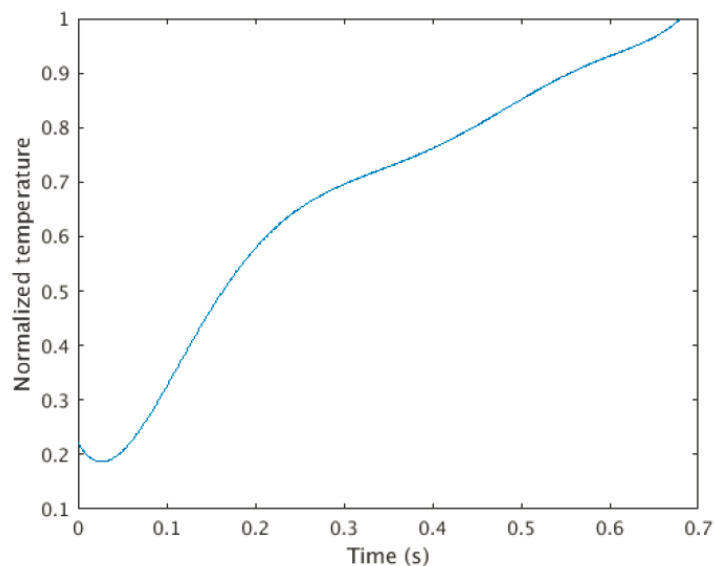
% Assigning the normalized starting temperature in the first position
in a
% vector
discrete_values(1)=29.896/temp(681);

% For-loop to assign all normalized temperature values in a vector
for i=1:1:13
    x=round(681*discrete_step*i);
    discrete_values(i+1)=temp_scale(x);
end

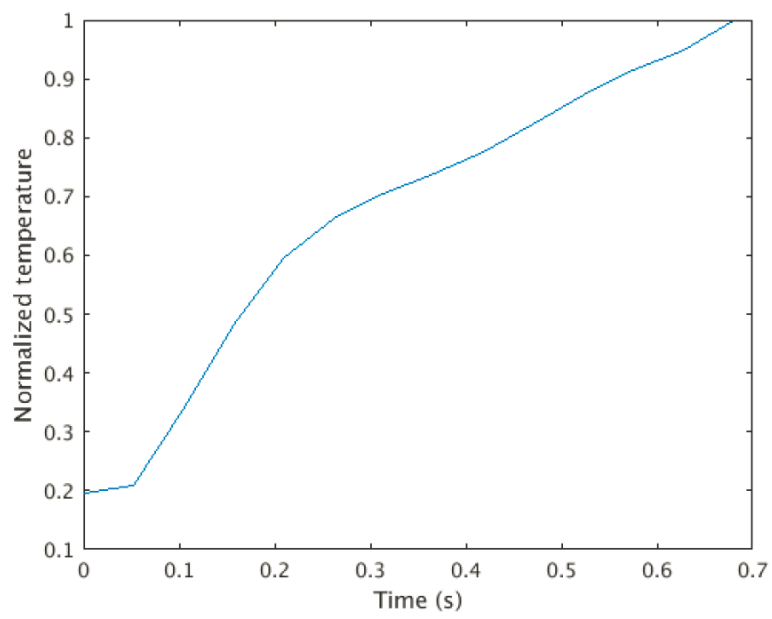
% Vector of the normalized time
y=[0:discrete_values*0.68:0.68];

```

(a) Code in MATLAB for plotting the approximated function of the temperature of a specific node on the top of the packaging material and extracting the values used in HyperMesh.



(b) Plot of the approximated function described in (a). The normalized temperature is plotted w.r.t. time.



(c) Plot of the actual temperature curve used.

Figure A.1

```
1 from abaqus import *
2 from abaqusConstants import *
3 import __main__
4 import datetime
5
6 def color_macro():
7     import section
8     import regionToolset
9     import displayGroupMdbToolset as dgm
10    import part
11    import material
12    import assembly
13    import step
14    import interaction
15    import load
16    import mesh
17    import optimization
18    import job
19    import sketch
20    import visualization
21    import xyPlot
22    import displayGroupOdbToolset as dgo
23    import connectorBehavior
24    session.viewports[session.currentViewportName].enableMultipleColors()
25    session.viewports[session.currentViewportName].setColor(initialColor='#BDBDBD')
26    cmap = session.viewports[session.currentViewportName].colorMappings['Material']
27    cmap.updateOverrides(overrides={'Alu_foil':(True,
28        '#C8C8C8', 'Default', '#C8C8C8'), 'Paper_board':(True, '#924A17',
29        'Default', '#924A17'), 'Polymer':(True, '#0099FF', 'Default',
30        '#0099FF')})
31    session.viewports[session.currentViewportName].setColor(colorMapping=cmap)
32    session.viewports[session.currentViewportName].disableMultipleColors()
33
34
35 def Print_viewport():
36     import section
37     import regionToolset
38     import displayGroupMdbToolset as dgm
39     import part
40     import material
41     import assembly
42     import step
43     import interaction
44     import load
45     import mesh
46     import optimization
47     import job
48     import sketch
49     import visualization
50     import xyPlot
51     import displayGroupOdbToolset as dgo
52     import connectorBehavior
53
54     #Create variables containing path, odb-name
55
56     path=session.viewports[session.currentViewportName].displayedObject.name
57
58     odb_full_name=path.split('/')[-1]
59
60     odb_name=odb_full_name.split('.')[0]
61
62
63     #Creating time-stamp for image export
64
65     temp=datetime.datetime.now()
66     year=str(temp.year)+'_'
67     month=str(temp.month)+'_'
68     day=str(temp.day)+'_'
69     hour=str(temp.hour)+'_'
70     minute=str(temp.minute)+'_'
71     second=str(temp.second)
72     time= year+month+day+hour+minute+second
```

```

73
74
75     #Printing the image to a file containing the .odb-file's name as well as a
       time-stamp, to prevent overwriting
76
77     session.printToFile(fileName=(odb_name + '_' + time) , format=PNG,
       canvasObjects=(session.viewports[session.currentViewportName], ))
78
79
80     def viewpoint():
81         import section
82         import regionToolset
83         import displayGroupMdbToolset as dgm
84         import part
85         import material
86         import assembly
87         import step
88         import interaction
89         import load
90         import mesh
91         import optimization
92         import job
93         import sketch
94         import visualization
95         import xyPlot
96         import displayGroupOdbToolset as dgo
97         import connectorBehavior
98
99     #Adjusting the window to obtain the same view for all images, to better be able
       to compare them
100
101
102     session.viewports[session.currentViewportName].view.setValues(nearPlane=0.0447878,
103
104         farPlane=0.055223, width=0.0190509, height=0.0111325,
       viewOffsetX=-0.00392375, viewOffsetY=0.000437315)
105
106     session.viewports[session.currentViewportName].view.setValues(nearPlane=0.0449539,
107
108         farPlane=0.0527813, width=0.0191216, height=0.0111739, cameraPosition=(
       0.00478146, -0.0184407, -0.0453952), cameraUpVector=(0.106816,
       -0.919275, 0.378846), cameraTarget=(0.000727064, 0.000284987,
       0.00118589), viewOffsetX=-0.00393831, viewOffsetY=0.000438938)
109
110     session.viewports[session.currentViewportName].view.setValues(nearPlane=0.0449485,
111
112         farPlane=0.0527867, width=0.0191194, height=0.0111726,
       viewOffsetX=-0.00250616, viewOffsetY=0.000738382)
113
114     session.viewports[session.currentViewportName].view.setValues(nearPlane=0.0447428,
115
116         farPlane=0.0529923, width=0.0221287, height=0.0129311,
       viewOffsetX=-0.00288752, viewOffsetY=0.000772681)
117
118     session.viewports[session.currentViewportName].view.setValues(nearPlane=0.0447277,
119
120         farPlane=0.0530075, width=0.0221212, height=0.0129267,
       viewOffsetX=-0.0013355, viewOffsetY=0.000968278)
121
122     session.viewports[session.currentViewportName].view.setValues(nearPlane=0.0443539,
123
124         farPlane=0.0539321, width=0.0219363, height=0.0128187, cameraPosition=(
       -0.00574675, -0.0209342, -0.0443852), cameraUpVector=(0.115538,
       -0.906146, 0.406878), cameraTarget=(0.00103038, 0.000226384,
       0.0008164), viewOffsetX=-0.00132434, viewOffsetY=0.000960186)
125
126     session.viewports[session.currentViewportName].view.setValues(nearPlane=0.0403714,
127
128         farPlane=0.0587754, width=0.0199667, height=0.0116677, cameraPosition=(
       -0.0243181, -0.0187468, -0.0389103), cameraUpVector=(0.284441,
       -0.921914, 0.263), cameraTarget=(0.00105558, 0.000248662, 0.000233435),
       viewOffsetX=-0.00120543, viewOffsetY=0.000873971)

```

Figure A.2: Scripts for Abaqus, written in Python.